Chemical Engineering Journal 430 (2022) 132639

Contents lists available at ScienceDirect

Chemical Engineering Journal

journal homepage: www.elsevier.com/locate/cej

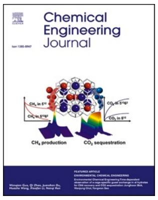

A Novel ceramic tubular membrane coated with a continuous graphene-TiO_2 nanocomposite thin-film for CECs mitigation

Pedro H. Presumido [a], Lucrécio F. dos Santos [b], Teresa Neuparth [c], Miguel M. Santos [c,d], Manuel Feliciano [e], Ana Primo [f], Hermenegildo Garcia [f], Maja B- Đolić [g], Vítor J.P. Vilar [a,*]

[a] Laboratory of Separation and Reaction Engineering-Laboratory of Catalysis and Materials (LSRE-LCM), Department of Chemical Engineering, Faculty of Engineering, University of Porto, Rua Dr. Roberto Frias, 4200-465, Porto, Portugal
[b] Chemical Engineering Department, Engineering School of Lorena, University of São Paulo, Estrada Municipal do Campinho s/n, 12602-810, Lorena, Brazil
[c] CIMAR/CIIMAR – Interdisciplinary Centre of Marine and Environmental Research, University of Porto, Group of Endocrine Disruptors and Emerging Contaminants, Avenida General Norton de Matos, S/N, 4450-208, Matosinhos, Portugal
[d] FCUP – Department of Biology, Faculty of Sciences, University of Porto, Rua do Campo Alegre, 4169-007, Porto, Portugal
[e] Centro de Investigação de Montanha (CIMO), Instituto Politécnico de Bragança, Campus de Santa Apolónia, 5300-253, Bragança, Portugal
[f] Instituto de Tecnología Química CSIC-UPV, Universitat Politècnica de València, Consejo Superior de Investigaciones Científicas, Av. de los Naranjos s/n, 46022, Valencia, Spain
[g] Faculty of Technology and Metallurgy, University of Belgrade, Karnegijeva 4, 11000, Belgrade, Serbia

ARTICLE INFO

Keywords:
Photocatalytic membrane reactor
Nano-engineered membrane
Membrane fouling
Continuous photocatalytic thin-film
Contaminants of emerging concern

ABSTRACT

This work presents a ceramic tubular membrane coated with a continuous graphene-TiO_2 nanocomposite thin-film for contaminants of emerging concern (CECs) removal from synthetic and real matrices in single-pass flow-through operation. Microfiltration ceramic membranes were coated *in situ* with graphene (G)-TiO_2-P25 nano-composite using two different methods: Membrane type A - TiO_2-P25 incorporated in the G preparation stage (1% [MA-1], 2% [MA-2] and 3% [MA-3] [w/v]), and Membrane type B - TiO_2-P25 thin-film uniformly coated over the G film surface (coating layers: 3 [MB-1], 6 [MB-2], and 9 [MB-3]). After the catalyst deposition and before the pyrolysis step, air was forced to pass through the membranes pores (inside-outside mode), providing a porous film. The CECs solution (diclofenac-DCF, 17β-estradiol-E2, 17α-ethinylestradiol-EE2 and amoxicillin-AMX) was prepared using Ultrapure water (UPW) or an urban wastewater after secondary treatment (UWW) fortified with 500 $\mu g\ L^{-1}$ of each CEC. Membranes were characterized by the following techniques: Scanning Electron Microscopy (SEM), Atomic Force Microscopy (AFM), Fourier-Transform Infrared spectroscopy (FTIR), Diffuse Reflectance UV-Visible spectroscopy (DR UV-Vis) and Raman spectroscopy. The membranes coated with MA-3 and MB-2 catalyst films, irradiated by UVA light, showed the highest ability for CECs removal. Furthermore, the Relative flux reduction ratio (RFR) decreased around 45% in the absence of UVA light, owing to membrane fouling. The combination of filtration and oxidation (G-TiO_2-UVA) provided a permeate with higher quality and minimized membrane fouling. Although membrane type B allowed for a permeate with higher quality, membrane type A provided a higher permeate flux.

1. Introduction

Urban wastewater treatment plants (UWWTPs) are the major hotspots for contaminants of emerging concern (CECs) (e.g. pharmaceutically active compounds, pesticides, industrial chemicals, etc.), antibiotic resistant bacteria (ARB) and antibiotic resistance genes (ARGs), release to water compartments, and, consequently, new approaches are required to reduce CECs&ARB&ARGs mass fluxes into the environment, towards One Water – One Health approach [1]

The European Parliament recently approved the minimum requirements at the European level for the first time for reclaimed water (i.e., urban wastewater that has been treated in a reclamation plant) to be used for agricultural purposes, in a safe way, protecting people and the environment [2]. Due to its high separation efficiency, membrane filtration, specially nanofiltration and reverse osmosis, is an up-and-coming technology for tertiary treatment of urban wastewaters,

---

* Corresponding author.
E-mail address: vilar@fe.up.pt (V.J.P. Vilar).

https://doi.org/10.1016/j.cej.2021.132639
Received 9 May 2021; Received in revised form 21 September 2021; Accepted 22 September 2021

towards CECs&ARB&ARGs removal, achieving a permeate with high quality, safe to be reused in agriculture irrigation [3–5]. However, disposal of concentrate waste stream, high energy requirements, low permeate flux, low selectivity and fouling, constitute significant obstacles to broader implementation in UWWTPs [6,7]. Thus, the use of photocatalytic membrane reactors (PMRs) may appear as a very promising solution. PMRs are hybrid systems coupling photocatalysis with membrane filtration in a single unit [8,9]. The main action mechanisms of PMRs are CECs&ARB&ARGs retention and oxidation. The generation of highly reactive oxygen species (e.g. $OH^{\bullet}$ and $O_2^{-\bullet}$ radicals) on the membrane surface are able to: i) enhance membrane permeability and hydrophilicity and ii) improve the antifouling membrane properties through oxidation of organic molecules, and microbiota adsorbed onto the membrane surface and blocking the membrane pores, leading to a higher and more constant permeate flux and a concentrate with higher quality [6,10–12]. Additionally, CECs&ARB&ARGs are forced towards the membrane surface, increasing its concentration near the liquid/catalyst interface, boosting the reaction rate.

Although semiconductors, such as TiO_2-P25, can be anchored on ceramic membranes to improve its performance (nano-engineered membrane) [8,13], the high recombination rate of photogenerated e^-/h^+ is a major drawback [14]. Graphene (G) is a single layer of a carbon hexagonal network showing a high surface area with delocalization of π electrons, boosting the charge carrier's separation in photocatalytic reactions. G-based TiO_2 membrane for CECs&ARB&ARGs removals has recently been reported elsewhere [15–17]. Almeida et al. [18] reported TiO_2/graphene oxide (GO) nanocomposite immobilized into poly (vinylidene difluoride-co-trifluoroethylene) (P(VDF-TrFE)) fibers, showing high oxidation rates for methylene blue. Rao et al. [19] fabricated a flat membrane interconnecting TiO_2 nanowires, Fe_2O_3 nanoparticles, and GO sheets for the removal of humic acids from water. All these studies used flat-shaped membranes and a great majority of G-based TiO_2 membranes are porous polymeric supported (e.g., polyvinylidene fluoride, PVDF; polysulfone, PSF; polypropylene, PP; and polyacrylonitrile, PAN) [20–23]. Moreover, among the significant number of publications on photocatalytic membranes with G-based, only a few are related to ceramic tubular membranes [24–26].

Until now, a significant amount of G-TiO_2 composites have been prepared through various techniques using more than one stage without achieving a continuous G layer in the membrane [27–29]. Moreover, most of them have several limitations, either in the membrane area or in the need to prepare highly expensive chemical vapor deposition (CVD) graphene and subsequent transfer graphene to the membrane surface. Therefore, the method of preparing graphene-based membranes is the key to the large-scale fabrication of nanosheet membranes on tubular substrates for industrial applications. In a previous work of our research team, a ceramic membrane doped with a continuous graphene layer was fabricated in a single pyrolysis step, using chitosan as precursors of G, and applied for salt rejection [30].

Hence, this work reports for the first time a ceramic tubular membrane coated with a continuous G-TiO_2 nanocomposite thin-film for CECs removal from synthetic and real matrices in single-pass flow-through operation. The functionalization of the microfiltration membranes (MFs) was optimized using two different methods to verify which is the best option regarding the quality and quantity of the permeate: A) TiO_2-P25 incorporated in the preparation stage of G, and B) TiO_2-P25 deposited over the G layer. The photocatalytic membranes were assembled in a PMR, having an outer borosilicate tube as reactor window, and UVA lamps located around the window, and further tested for the removal of a mixture of four CECs (diclofenac-DCF, 17β-estradiol-E2, 17α-ethinylestradiol-EE2 and amoxicillin-AMX) using Ultrapure water (UPW) or Urban wastewater (UWW) after secondary treatment, as reaction matrices.

Table 1
Summary of membrane nomenclature.

Membrane	Fabrication conditions	Nomenclature
Membrane type A *TiO_2-P25 incorporated in the G preparation stage*	CS + 1% of TiO_2-P25 + pyrolysis	MA-1
	CS + 2% of TiO_2-P25 + pyrolysis	MA-2
	CS + 3% of TiO_2-P25 + pyrolysis	MA-3
Membrane type B *TiO_2-P25 thin-film uniformly coated over the G film surface*	CS + pyrolysis + 3 coating layers (TiO_2-P25)	MB-1
	CS + pyrolysis + 6 coating layers (TiO_2-P25)	MB-2
	CS + pyrolysis + 9 coating layers (TiO_2-P25)	MB-3

*Note: CS – Chitosan; G – Graphene.

2. Materials and methods

2.1. Chemicals

Amoxicillin (AMX, MW = 365.40 g mol^{-1}, CAS# 26787–78-0), diclofenac sodium salt (DCF, MW = 318.13 g mol^{-1}, CAS# 15307–79-6), 17β-estradiol (E2, MW = 272.38 g mol^{-1}, CAS# 50–28-2) and 17α-ethinylestradiol (EE2, MW = 296.403 g mol^{-1}, CAS# 57–63-6) were supplied by Sigma-Aldrich. A CECs stock solution (500 mg L^{-1}) was prepared by dissolving AMX/DCF/E2/EE2 in acetonitrile (Fisher Chemical^{TM}) followed by gradual dilution with ultrapure water (UPW), resulting in an acetonitrile content of 16% (v/v). TiO_2 Aeroxide® P25 (Evonik, Germany, ≥ 99.5% (w/w) purity, 80% anatase and 20% rutile crystalline phases, average crystal size of 25 nm, specific surface area of 50 m^2 g^{-1}, and density of 3.9 g cm^{-3}) was used as photocatalyst. The surfactant Triton^{TM} X-100 was purchased from Sigma-Aldrich and used in the preparation of the TiO_2-P25 suspension for membrane coating. Chitosan (CS) from Sigma-Aldrich (low molecular weight) was used as a precursor to graphene films. For AMX, DCF, E2 and EE2 determination by HPLC-DAD, acetonitrile and methanol obtained from Fisher Chemical^{TM} and oxalic acid dehydrate (100%) from Panreac Quimica SLU were used as mobile phases. AvistaClean® P611 (Avista Technologies, United Kingdom) solution was used to clean the membrane after each experiment. UPW (Millipore Direct-Q®, 18.2 MΩ cm^{-1} at 25 °C) was used to prepare eluents and CECs solutions, as also for membrane cleaning before each experiment and permeability tests. To evaluate the photonic flow, 2-Nitrobenzaldehyde-2NB (99% purity) provided by Labbox Labware, S.L was used. A non-photoactive microfiltration α-Al_2O_3 membrane (outside-inside filtration mode) with 100 nm pore size (40–55% porosity), an outside diameter of 2 cm, internal diameter of 1.6 cm, length of 20 cm and effective membrane area of 84 cm^2 was purchased from Inopor®, Germany.

2.2. Fabrication of continuous G-TiO_2 thin-films on membrane shell-side

Continuous multi-layer defective G-TiO_2 thin-films over the ceramic membrane shell-side were prepared *in situ* following the procedure detailed described in Presumido et al. [30]. A CS solution was prepared by adding slowly 5 g of CS in 250 mL of UPW acidified with acetic acid (25%). A photocatalyst aqueous suspension was prepared by adding 5 g of TiO_2-P25 powder and two drops of TritonTM X-100 in 250 mL of UPW.

G-TiO_2 nanocomposite thin-films were prepared using two methods: (A) TiO_2-P25 incorporated in the G preparation stage, and (B) TiO_2-P25 thin-film uniformly coated over the G film surface (Table 1). For membrane type A, different amounts of TiO_2-P25 (1% [MA-1], 2% [MA-2] and 3% [MA-3] [w/v]) were added to the CS solution. For values higher than 4% w/v, the film was not continuous. A detachment and peeling off of the resulting G-TiO_2 film from the alumina membrane was visibly observed. Hence, a maximum of 3% TiO_2 (w/v) was used in this work. Before use, the prepared suspensions were magnetically stirred for 24 h and sonicated for 15 min at 50 kHz. The prepared suspensions were used to coat the membrane shell-side with one immersion using a dip-coating method with an immersion rate and withdrawing speed of 8 cm min^{-1} and an immersion time of 1 min (Dip-Coater RDC 15, Bungard Elektronik GmbH & Co. KG). The G-TiO_2 decorated membrane was dried by placing it in a horizontal position over a heating plate at 100 °C for 30 min, at a rotation speed of 40 rpm, followed by another 30 min in an oven at 100 °C. Subsequently, the membranes were subjected to compressed air flow (inside-outside mode) at 5 bars for 10 min, providing a physical opening of the pores. Then, the membrane with CS-TiO_2-P25 film was pyrolyzed under argon flow (300 mL min^{-1}), at a heating rate of 5 °C min^{-1} until reaching 600 °C for 4 h [31]. Insert Table 1

For the preparation of membrane type B, the same procedure described above was repeated using a CS solution without TiO_2-P25; after which, the G-decorated membrane was immersed in a TiO_2-P25 solution using the same dip-coating procedure. Following each immersion, the membrane was dried in an oven at 100 °C for about 15 min and this procedure was repeated (coating layers: 3 [MB-1], 6 [MB-2], and 9 [MB-3]) until achieving the desired mass of the catalyst on the membrane surface (17, 24 and 30 mg of TiO_2).

Regardless of the deposition method (A or B), the membrane functionalized with G-TiO_2 was inserted into the reactor and cleaned through the permeation of UPW for 1 h. The total mass of catalyst deposited on the membrane was calculated by weighing the membrane prior to catalyst deposition and after the cleaning and drying process. Furthermore, the membranes before and after the reactions were weighed (dry mass) to measure the possible leaching of TiO_2, and the difference was$<$1% of the total mass of TiO_2. Also, the absorbance of the concentrate and permeate streams at 500 nm, characteristic of TiO_2, was negligible during the reaction period.

2.3. Characterization techniques

Raman spectra were recorded at room temperature with a Horiba Jobin YvonLabram HR UV–Visible–NIR (200 – 1600 nm) Raman Microscope Spectrometer, using a 632 nm laser as the excitation source. Raman spectra were recorded in random points of a 1 × 1 cm^2 film.

The morphology of the sample was analyzed by Scanning electron microscopy (SEM) using a JEOL JSM 6300 apparatus equipped with an X-MAX detector of Oxford Instruments and coupled with energy dispersive X-ray (EDS) analysis. To determine the surface porosity and pore size distribution on the G-TiO_2 functionalized samples, SEM images from randomly chosen area (around 100 points) were analyzed by Image Pro software. The textural properties of tested samples were analyzed using liquid nitrogen porosimetry or the Brunauer-Emmett-Teller (BET) adsorption-desorption isotherms, measured by Micrometrics ASAP 2020 V 1.05H surface area analyzer.

The surface morphology was investigated by Atomic force microscopy (AFM) with NanoScope 3D (Veeco, USA) microscope operated in taping mode under ambient conditions. Etched silicon probes with spring constant 20 – 80 Nm^{-1} were used. Image analysis was done by Nanoscope image processing software. The Roughness surface morphology (RSM) is calculated as the root mean square average of height deviations taken from the mean data plane (Eq. (1)):

$$\mathrm{RSM} = \sqrt{\frac{\sum Z_i^2}{n}} \quad (1)$$

where Z_i is the maximum vertical distance between the highest and lowest data points in the image.

Fourier Transform Infrared spectra (FTIR) of samples were recorded on ATR-FTIR Nicolet iS10 (Thermo Scientific) spectrometer in the range 4000–500 cm^{-1} with a resolution of 4 cm^{-1} and at room temperature. The UV–Visible diffuse reflectance spectra (DRS) were recorded on a Shimadzu 2600 UV–Visible spectrometer with an integrating sphere attachment within the wavelength range from 200 to 700 nm. An Attension Theta optical tensiometer with automated liquid pumping system was used for the contact angle measurements. UPW was used as the probe liquid.

The point of zero charge (pH_{pzc}) of the G-TiO_2 film was determined following a pH drift test as described elsewhere [32]. Briefly, an amount (5 mL) of 0.01 M NaCl solution was placed in a flask and the pH was adjusted to a value between 2 and 10 by addition of 0.01 M HCl or 0.01 M NaOH. Then, 15 mg of G-TiO_2 film powder was added and the final pH was measured after 24 h under stirring at room temperature. After the shaking process, the final pH of suspensions was recorded. The difference between final and initial pH value (ΔpH) was plotted against initial pH. The point of intersection of the resulting curve at with $\Delta pH = 0$ gives the value of pH_{pzc}.

X-ray powder diffraction (XRD) data for the quantitative phase analysis were acquired on a Shimadzu XRD-7000 diffractometer with a Cu Kα radiation (40 kV and 30 mA).

2.4. Preliminary photocatalytic tests in a batch reactor

As there is an impossibility to compare G-TiO_2 membranes with a TiO_2 membrane in continuous filtration mode, since there are significant differences in size and distribution of the pores (discussed in more detail in section 3.1), batch tests were carried out to evaluate the oxidation ability of the different catalyst thin-films over the membrane shell-side. Hence, a tubular MF membrane was cut into small pieces of 1 cm in length. G-TiO_2 and TiO_2 films were produced on the external surface of the small pieces of MF membrane using the methods described in Section 2.2. Under batch conditions, the following catalyst films/system were tested and compared towards CECs oxidation: pristine membrane piece, G membrane piece, UVA + pristine membrane piece, UVA + G membrane piece, UVA + TiO_2 membrane piece, and UVA + G-TiO_2 membrane pieces (Membranes type A or B).

The batch experimental system was composed mainly of a 200 mL thermostatic glass vessel, a magnetic stirrer, and a UVA lamp (Philips TL 6 W, $\lambda_{max} = 365$ nm) located above the vessel. 150 mL of CECs solution prepared with UPW ([CEC]0 = 500 μg L^{-1} of each) was added to the vessel (25 °C) and mixed by magnetic stirring. The MF membrane piece was inserted in the bottom of the vessel. CECs adsorption on the catalyst film was evaluated during 10 min and, immediately afterwards, the UVA lamp was switched on, starting the reaction for 180 min. CECs photolysis was evaluated in the absence of the membrane pieces. Samples were collected at a predefined series of time intervals and then analyzed in terms of CECs concentration.

2.5. Photocatalytic membrane reactor's setup and experimental procedure

The lab-scale system integrates: i) a photocatalytic membrane reactor (vertical position) equipped with four UVA lamps (Philips TL 6 W, $\lambda max = 365$ nm, photonic flux of 1.19 ± 0.02 J $s^{-}1$) located externally to the reactor window; ii) a 5 L feed tank (cylindrical glass vessel) coupled to a thermostatic bath (Julabo, model F12-EH) and a magnetic stirrer (CAT, model M5); iii) a gear pump (Tuthill Pump Group, DGS.68) to feed the membrane module; iv) a system to control the pump, lights and flow rate, and v) a back pressure regulator (BPR) connected to a personal computer to regulate the transmembrane pressure. The PMR unit comprises an inner-tubular ceramic membrane and an outer borosilicate glass tube (length: 15.5 cm; internal diameter: 6 cm; thickness: 9 cm; maximum pressure: 12.5 bar), as reactor window, allowing UVA light to penetrate into the annular reaction zone until the membrane surface. Polytetrafluoroethylene (PTFE) tubes were used to connect the whole system units (Fig. S1).

First, the feed tank was filled with 5 L of CECs solution, which was maintained at 25 °C. The CECs solutions were prepared using UPW or

Table 2
Main physicochemical characteristics of the urban wastewater (UWW) collected after secondary treatment in a UWWTP (Northern Portugal).

Parameter (units)	Values
Color	Pale yellow
pH	7.2
Temperature (°C)	16.7
Conductivity (μS cm^{-1})	198
Turbidity (NTU)	0.9
Absorbance at 254 nm (AU)	0.15
Transmittance at 254 nm (%)	70.8
Dissolved organic carbon (mg L^{-1})	6.2
Dissolved inorganic carbon (mg L^{-1})	2.9
Chemical oxygen demand (mg O_2 L^{-1})	26
Total dissolved iron (mg L^{-1})	0.2
Total suspended solids (mg L^{-1})	1.5
Volatile suspended solids (mg L^{-1})	0.5
Total nitrogen (mg L^{-1})	35
Total phosphorous (mg L^{-1})	1.9
Nitrite – N-NO_3^- (mg L^{-1})	0.1
Sulfate – SO_4^{2-} (mg L^{-1})	19.0
Chloride – Cl^- (mg L^{-1})	17.4
Bromide – Br^- (mg L^{-1})	< 0.08[a]
Fluoride – F^- (mg L^{-1})	< 0.03[a]
Phosphate – PO_4^{3-} (mg L^{-1})	<0.5[b]
Sodium – Na^+ (mg L^{-1})	0.93
Ammonium – NH_4^+ (mg L^{-1})	< 0.02[a]
Potassium – K^+ (mg L^{-1})	5.2
Magnesium – Mg^{2+} (mg L^{-1})	1.7
Calcium – Ca^{2+} (mg L^{-1})	15.4

[a] Limit of detection.
[b] Limit of quantification.

UWW fortified with the same amount of CECs ($[CEC]0 = 500$ μg L¯1 of each). No pH correction was performed for the UWW fortified with CECs. The main characteristics of the UWW sample are presented in Table 2. Insert Table 2

The CECs adsorption on the membrane surface was evaluated for 30 min (without permeation), in which the solution passed through the entire system in dark (recirculation mode). Immediately, the cross-flow velocity (CFV) and the transmembrane pressure (TMP) was set to 0.01 m s^{-1} and 10 bar, respectively, and the UVA lamps were switched on, starting the reaction time. The CECs solution filtration was carried out in outside-inside mode. Prior to the photocatalytic experiments, all membranes were firstly stabilized with UPW filtration (J_0) water at a TMP of 10 bar for 1 h. The membrane's permeability was evaluated using UPW at multiple TMP (3, 6, 10 bar). The permeate flux (J_{CECs}) was determined through collecting a volume of permeate during a certain period of time. Samples were collected at predefined times (0, 15, 30, 45, 60, 90, 120, 150, 180, 210 min). The retentate was continuously recirculated to the feed tank. Permeate samples were collected under time intervals until steady-state conditions (90 min) were achieved and then analyzed in terms of CECs.

In order to investigate the antifouling properties of the G-TiO_2 membranes, the Flux recovery ratio (FRR), the Relative flux reduction ratio (RFR), reversible fouling ratio (Rr) and irreversible fouling ratio (Rir) were determined. After the experiment, the membranes were washed with UPW for 1 h to remove loosely attached organics. Then, the flux of the cleaned membrane (J_{CM}) was measured again at 10 bar. The FRR (Eq. (2)), RFR (Eq. (3)), Rr (Eq. (4)) and Rir (Eq. (5)) were calculated as follows [33]:

$$\mathrm{FRR}(\%) = \left(\frac{J_{CM}}{J_0}\right) \times 100 \tag{2}$$

$$\mathrm{RFR}(\%) = \left(\frac{J_0 - J_{CECs}}{J_0}\right) \times 100 \tag{3}$$

$$\mathrm{Rr}(\%) = \left(\frac{J_{CM} - J_{CECs}}{J_0}\right) \times 100 \tag{4}$$

$$\mathrm{Rir}(\%) = \left(\frac{J_0 - J_{CM}}{J_0}\right) \times 100 \tag{5}$$

The photonic flow was determined by the actinometry of 2NB (10 mM) [34]. 2 L of 2NB solution was placed in the reactor vessel, recirculated in all system for 10 min in the dark, and a control sample was taken. After, the 4 UVA lamps were turned on and samples were collected at predefined times (0, 7.5, 15, 22.5, 30, 37.5, 45 min). The BPR was fully open, and no permeation occurred.

2.6. *Analytical determinations*

The CECs concentrations were followed by a reversed-phase HPLC using a VWR Hitachi ELITE LaChrom equipped with a Merck LiChrosorb® RP-18 (5 μm) LiChroCART® 125–4 column and a L-2455 diode array detector (DAD). An isocratic elution (48:52 (v/v) acetonitrile/ 0.014 M oxalic acid) was used for E2, EE2 and DCF determination. For the AMX quantification, the equipment was operated in a gradient mode using acetonitrile/methanol/0.014 M oxalic acid with ratios of 10:5:85 (v/v) from 0 to 3 min, 15:5:80 (v/v) from 3 to 5 min, 10:5:85 (v/v) from 5 to 8 min. The flow rate was set at 1.0 mL min^{-1}, the injection volume at 50 μL and DAD at 230 nm for AMX and 280 nm for E2, EE2 and DCF. The retention times for E2, EE2, DCF and AMX were 4.0 min, 5.1 min, 9.4 min and 3.3 min, giving detection limits of 7.86 μg L^{-1}, 18.8 μg L^{-1}, 15.2 μg L^{-1} and 10.7 μg L^{-1}, respectively. The 2NB concentration was determined using an isocratic elution with 60% 0.014 M oxalic acid/ 40% acetonitrile, at a flow rate of 0.60 mL min^{-1}. The retention time and the detection limit were 7.6 min and 2.4 mg L^{-1}, respectively.

Turbidity, total nitrogen, total phosphorous, total dissolved iron, chemical oxygen demand, total suspended solids, volatile suspended solids were all determined according to the Standard Methods [35]. The total dissolved carbon and dissolved inorganic carbon were measured in a Shimadzu TOC-V_{CSN} analyzer (Shimadzu, Kyoto, Japan). pH and temperature were measured using a Hanna Instruments HI-2020 edge® hybrid. Conductivity was determined by Hanna Instruments HI9828 multiparameter meter. The absorption spectra were evaluated between 200 and 800 nm using a Merck Spectroquant® Prove 300 UV/Vis spectrophotometer. Inorganic anions were analyzed by ion chromatography (Dionex ICS-2100 LC) equipped with an IonPac® AS11-HC 250 mm × 4 mm column ($T = 30$ °C) and an anion self-regenerating suppressor (ASRS® 300, 4 mm) under an isocratic elution of 30 mM KOH at a flow rate of 1.5 mL min^{-1}. Inorganic cations were also evaluated by ion chromatography in a Dionex DX-120 LC coupled with an IonPac® CS12A 250 mm × 4 mm column at ambient temperature and a CSRS® Ultra II cation self-regenerating suppressor (4 mm) under an isocratic elution of 20 mM methanesulfonic acid at a flow rate of 1.0 mL min^{-1}.

2.7. *Pseudo-first-order kinetic model fitting*

A pseudo-first-order model (Eq. (6)) was fitted to experimental data of CECs oxidation in the batch system, as a simple mathematical model, using a nonlinear regression method (Fig. P software for Windows from Biosoft).

$$[\mathrm{CEC}]_t = [\mathrm{CEC}]_0 \times e^{-k_{CEC} \times t} \tag{6}$$

where $[CEC]_t$ and $[CEC]_0$ are CEC concentration (μM or μg L^{-1}) after a certain time (t) and just before reaction beginning ($t = 0$), respectively, and k_{CEC} (min^{-1}) is the pseudo-first-order kinetic constant. The goodness of fitting was evaluated considering the relative standard deviations, the residual variance (S^2_R) and coefficient of determination (R^2).

2.8. *Toxicity screening using zebrafish embryo bioassay*

The zebrafish embryo bioassay, carried out based on the OECD Fish Embryo Acute Toxicity (FET) Test 236 [36], was used to evaluate the competence of the ceramic tubular membranes coated with G-TiO_2 in reducing the toxicity of synthetic and real matrices fortified with four CECs. The zebrafish embryo bioassay involved ten different treatments: synthetic matrix (dechlorinated water - control), solvent control (acetonitrile in dechlorinated water; the percentage of acetonitrile is equal to amount in the CECs working solution), real matrix (UWWTP secondary effluent), real matrix + acetonitrile, and CECs in synthetic and real matrices before and after the treatment with the membranes.

2.8.1. *Zebrafish maintenance and eggs collection*

Adults zebrafish AB strain were kept in dechlorinated water at 28 ± 1 °C and under a photoperiod of 12:12 h (light:dark). Animals were fed ad libitum, twice a day, with commercial food Tetramin (Tetra, Melle, Germany), supplemented every two days with live *Artemia spp*. In order to induce zebrafish breeding, in the afternoon prior to the beginning of the embryo bioassay, adults in a proportion of 2:1 (male:female) were allocated in a breading box to reproduce. At the following day, 1.5 h after the beginning of the light period, newly fertilized eggs were collected and cleaned in order to start the embryo bioassay [37].

2.8.2. *Zebrafish embryo bioassay OECD 236*

The clean zebrafish eggs were observed in a magnifying glass and randomly allocated in 24-well plates (one embryo per well) previously incubated with 1.5 mL of each treatment. In each 24-well plate was assigned one treatment composed of 20 embryos divided into five replicates plus an internal plate control (4 embryos). The plates were randomly maintained in an incubator at 26 °C ± 0.5 for 96 h under the same photoperiod as the adults. The treatment solutions were renewed daily in order to maintain oxygen saturation and the integrity of the solutions. Embryos were checked every day for mortality and dead embryos were removed. Embryo development was checked under an inverted microscope (Nikon Eclipse 5100 T) coupled with a digital camera Nikon D5 – Fi2, and morphological abnormalities on the head, tail, notochord, pericardial and yolk-sac oedemas, and hatching rate were recorded as present or absent at 24, 48, 72, and 96 h post-fertilization (hpf) [37,38]. At each observation time point, the different abnormalities were grouped and presented as total abnormalities.

2.8.3. *Statistical analysis*

Data obtained during the embryo bioassay were computed in Statistica 12.5 (Statsoft, USA). Data were tested for homogeneity of variances using Leven's test and transformed if required. If the homogeneity of variances was met, a one-way ANOVA followed by Fisher's least significant difference (LSD) test was performed in order to evaluate differences between the CECs in synthetic/real matrices and the synthetic/real matrices without the CECs; as well as differences between the CECs in both matrices before and after treatment with membranes. If the homogeneity of variances was not met even after data transformation, data were analyzed by Kruskal–Wallis followed by Multiple Comparison Rank Test. Significant differences were set at $p < 0.05$.

3. Results and discussion

The best G-TiO_2 functionalized membranes towards CECs rejection and permeate quantity were MA-3 (membrane type A) and MB-2 (membrane type B) (see section 3.2.2). Therefore, the discussion on membrane characteristics and results is based on these two samples and compared to their respective controls - in the absence of light (MA-3_{UVAoff} and MB-2_{UVAoff}).

3.1. *Characterization of the catalyst film immobilized on the porous membrane*

The G-TiO_2 nanocomposite films were obtained through a facile and single-step method in which CS was used as a precursor to graphene production. The surface of the ceramic membrane modified with G-TiO_2

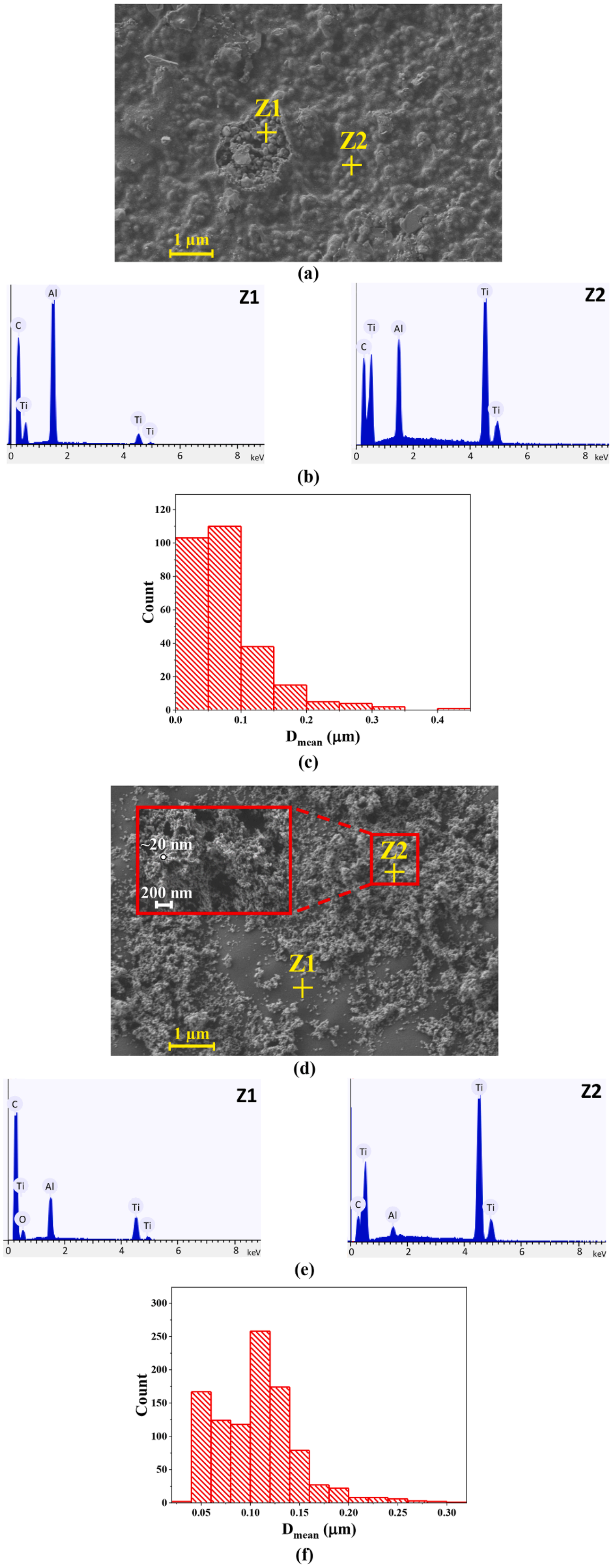

Fig. 1. SEM images of the top surface of the MA-3 (a) and MB-2 (d) modified membranes with the expected EDS spectra (b, e) and surface pore size distribution (c, f).

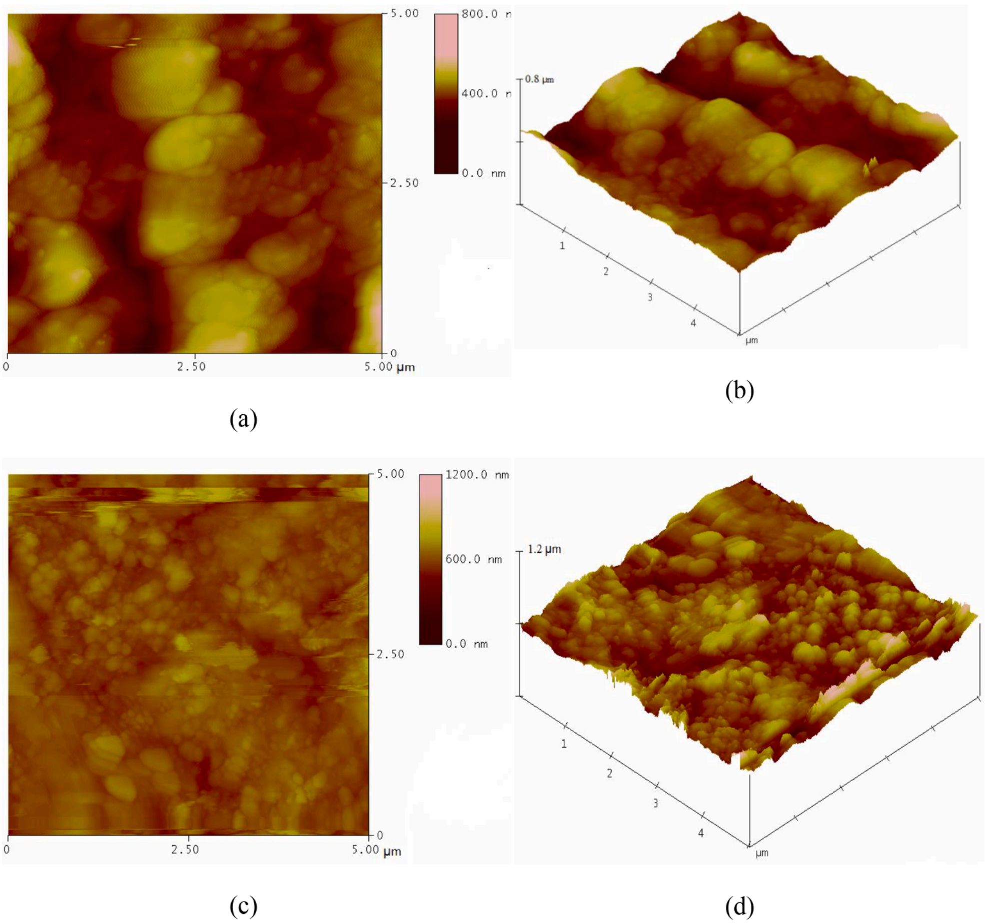

Fig. 2. Tapping mode AFM image of the sample MA-3: section 5 µm × 5 µm × 800 nm - top view image (a) and surface plot image (b); and the sample MB-2: section: 5 µm × 5 µm × 1200 nm - top view image (c) and surface plot image (d).

was wholly covered by a continuous film without the apparent presence of pinholes or cracks (Fig. 1). The preparation method for MA-3 resulted in a continuous film of G interspersed with aggregates of TiO_2, creating a discontinuity in the G layer, which allows more defects in the catalyst film (Fig. 1a). The image also shows that TiO_2 was bound together with G at the time of its formation by pyrolysis in an oxygen-free atmosphere. On the other hand, Fig. 1d (MB-2) shows a continuous G layer covered by TiO_2 nanoparticles. The surface morphology itself presented a slight agglomeration caused by the deposition of the photocatalyst over the G layer (Fig. 1d). Fig. 1a presents debris scratched from the graphene membrane to visually show a comparison between two different zones of the MA-3 film. From the analysis of EDS (Fig. 1b and 1e), the two different zones of the manufactured membranes indicate the presence of carbon, titanium and alumina, describing the materials of the G film, TiO_2 film and the ceramic membrane (α-Al_2O_3), respectively. The EDS results show the presence of carbon on the entire surface of the MA-3, even when zone Z2 is analyzed, which shows strong signs of the presence of both titanium and carbon. This indicates that G and TiO_2 are incorporated into each other. In contrast, for the manufacturing method of MB-2, the G film was coated with a TiO_2 layer. In zone Z2, where titanium is the predominant element, the TiO_2 film covers the G signal (Fig. 1e).

Hence, SEM analysis provides strong evidence that the G-TiO_2 was successfully prepared, in which the TiO_2 was bonded together with G film or coated over the G layer. This structure is beneficial for membrane fabrication as G can enhance the connection with TiO_2 and improve the strength of the membrane to be used as a barrier for the retention of CECs. In addition, the contact between G film and TiO_2 nanoparticles minimizes charge recombination, enhancing photocatalytic activity (see section 3.2.1). Insert Fig. 1

The comparison of the surface porosity and pore size distribution between the TiO_2-functionalized G samples (Fig. 1c and 1f) are set up to the following values: 1) the sample MA-3 showed a mean pore size of 67.3 nm with an average film porosity of 13.3%; and 2) the sample MB-2 presents a mean pore size of 48.4 nm with an average film porosity of 12.1%. Although the sample MB-2 presents a narrow pore size distribution than MA-3, both are classified as ultrafiltration membranes. In general, several ranges of G-TiO_2 micropores have been measured in the sample MB-2, making the catalyst surface more accessible/available for the solid–liquid interactions (i.e., the tendency of higher membrane fouling). The accumulation of the nanoparticles over the G film increases the surface roughness of membrane type B and subsequently reduces membrane fouling resistance.

The surface profile at the nanometer scale was effectively presented by the AFM technique. The top view image displays the selected image from a top-down perspective, where the height information is represented by the color at a given scale from 0.0 to 1200.0 nm, indicating generally low roughness of the sample MA-3 (Fig. 2a) and sample MB-2 (Fig. 2c). Surface Plot image displays the selected image with color-coded height information in a three-dimensional perspective (Fig. 2b and 2d). The Roughness surface morphology (RSM) for the sample MA-3 has shown higher homogeneity of the surface, with very similar RSM values for the sections of 5 µm × 5 µm × 800 nm ($RSM_{1\_5\mu m}$ = 52.9 nm, Fig. 2b) and 10 µm × 10 µm × 1500 nm ($RSM_{1\_10\mu m}$ = 75.39 nm – data not showed). The sample MB-2 has shown slightly higher roughness ($RSM_{2\_5\mu m}$ = 56.38 nm, Fig. 2d and $RSM_{2\_5\mu m}$ = 82.21 nm – data not shown). Additionally, the analytical AFM performance for the sample MB-2 was much more time/accuracy demanding, also indicating the

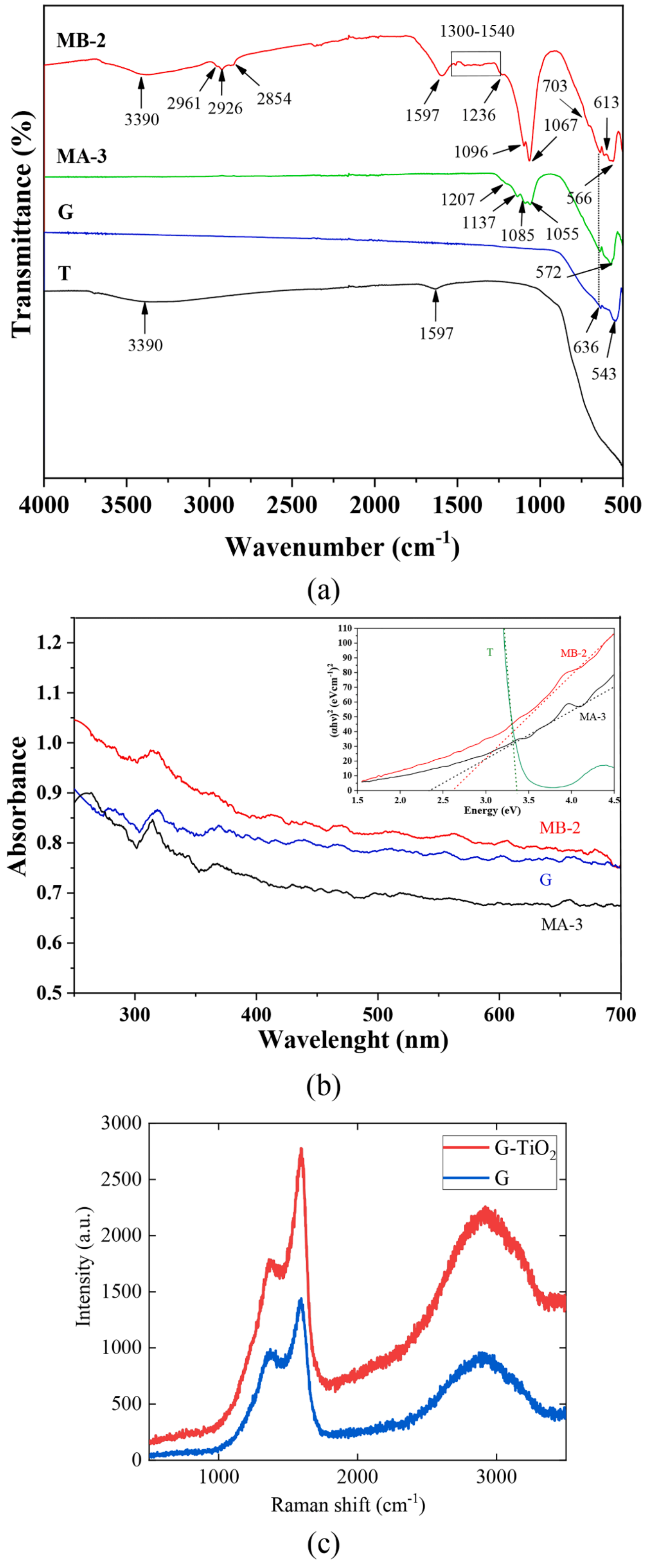

Fig. 3. (a) The FTIR spectra of graphene (G), TiO_2-P25 (T) and G-TiO_2-functionalized samples (MA-3 and MB-2); (b) The UV-Vis spectra of graphene (G) and G-TiO_2-functionalized samples (MA-3 and MB-2); the inset of panel (b) shows the bandgap energies of graphene (G), TiO_2-P25 (T) and G-TiO_2-functionalized samples (MA-3 and MB-2); (c) The RAMAN spectra of graphene and G-TiO_2-functionalized sample (MA-3).

higher roughness of the membrane surface.

Similar values of surface porosity and roughness of the tested materials (MA-3 and MB-2) are directly reflected in their analytical performances – both membranes resulted in the stabile structure with enhanced photocatalytic activity (section 3.2). The major difference in membranes' fabrication procedures is further demonstrated by the higher accessibility/availability of the TiO_2 active sites – manifesting the higher CECs abatement of the MB-2 sample (with TiO_2 thin-film layer). Insert Fig. 2

The FTIR spectra of G and G-TiO_2-functionalized samples (Fig. 3a) show the corresponding peaks at: 1055 cm^{-1} (C-O), 1067 cm^{-1}(C-O), 1085 cm^{-1} (C-O), 1137 cm^{-1} (C-OH), 1207 cm^{-1} (C-OH), 1236 cm^{-1} (C-OH) and 1597 cm^{-1} (C = C) [39–41]. The surface oxygen-containing functional groups render the possibility of covalent linkage of TiO_2 onto the G surface [42]. The intensities of those peaks are low for the MA-3 sample due to the influence of TiO_2 incorporated into CS before pyrolysis and, therefore, less exposure of the photocatalyst on the membrane surface. The peak at 3390 cm^{-1} originates from the hydroxyl group of water [39], which also demonstrates the hydrophilic surface of the MB-2 sample [43]. The bands at 2961, 2926 and 2854 cm^{-1} correspond to the C–H stretch vibrations of the methylene group [44]. The slight difference detected in the peak position for the tested samples is due to the difference in the degree of hydrogen bonding and other interactions [45]. The low peak of the lattice vibration of TiO_2 (Ti-O-Ti stretching) has been recorded in the wavelength of 703 cm^{-1} [40] and 1400 cm^{-1} [39] for the MB-2 sample. Moreover, Ti—O—C bond has been detected at a wavelength of 1096 cm^{-1} (MA-3) and 1085 cm^{-1} (MB-2) demonstrating an interaction between TiO_2 and G [41]; the Ti-element was dominantly present on the MB-2 surface of membrane (previously confirmed by the EDS technique).

The UV-Vis absorption spectra were measured in the diffuse reflection mode to access the optical absorption of composite material (Fig. 3b). An enhanced absorption capacity of the G-TiO_2 composites in the range of 200–700 nm is shown, and the absorption region is extended to the near-infrared region. The enhanced absorption of the G-TiO_2 composites is attributed to the presence of the Ti—C and Ti—O—C bonds. The characteristic absorption band of the graphene centered at 264 nm is attributed to the $\pi \rightarrow \pi^*$ transition of aromatic C—C bonds [46]. The shoulder present in the G-TiO_2-functionalized samples at 298 nm corresponds to the $n \rightarrow \pi^*$ transition of C═O bonds. The adsorption peak at 315 nm and 385 nm indicates the formation of continuous G-TiO_2 nanofilm [19,43]. It was observed that the peak position for the G-TiO_2-functionalized composites at 315 nm slightly shifted to 318 nm compared to the G. This redshift (of 3 nm) results from charge-transfer interactions between G and TiO_2, which is also confirmed by enhancing the Raman signal [47]. The bandgap energies, Eg (eV) of the MA-3 and MB-2 samples obtained from the Tauc Plot method [48], are 2.36 and 2.65 eV, respectively, much lower than that of the pure TiO_2 - 3.36 eV (mostly in the range of 3.1–3.4 eV) [49]. After the modification of TiO_2, the Eg is narrowed, and the light absorption range of TiO_2 can be extended into the visible region. The unique structure of the MA-3 facilitates the electron transfer due to the less exposed TiO_2 particles (i.e., graphene is providing the space separation of photoelectron and hole pairs in rapid electron transfer units), leading to the inhibition of the recombination of the e^-–h^+ pairs [43,50].

Raman spectroscopy was applied to determine the crystalline quality of the composite with continuous G-TiO_2 film – MA-3 (Fig. 3c). Two sharp picks have been detected for the G and G-TiO_2-functionalized sample: 1360 cm^{-1} for the D band (disorder carbon) and 1594 cm^{-1} for the G band (graphene carbon) [51]. D-band corresponds to the structural carbon disorders [40], while the G-band can be attributed to the first-order scattering of E_{2g} proton of SP^2 carbon atoms of graphene [52]. The crystal structure, disorder and defects may be further determined by the relative intensity of D and G peaks. The position of D- and G-band (Fig. 3c) is the same for both samples, where the higher intensity of peaks implies the density of structural defects in the G-TiO_2 sample (MA-

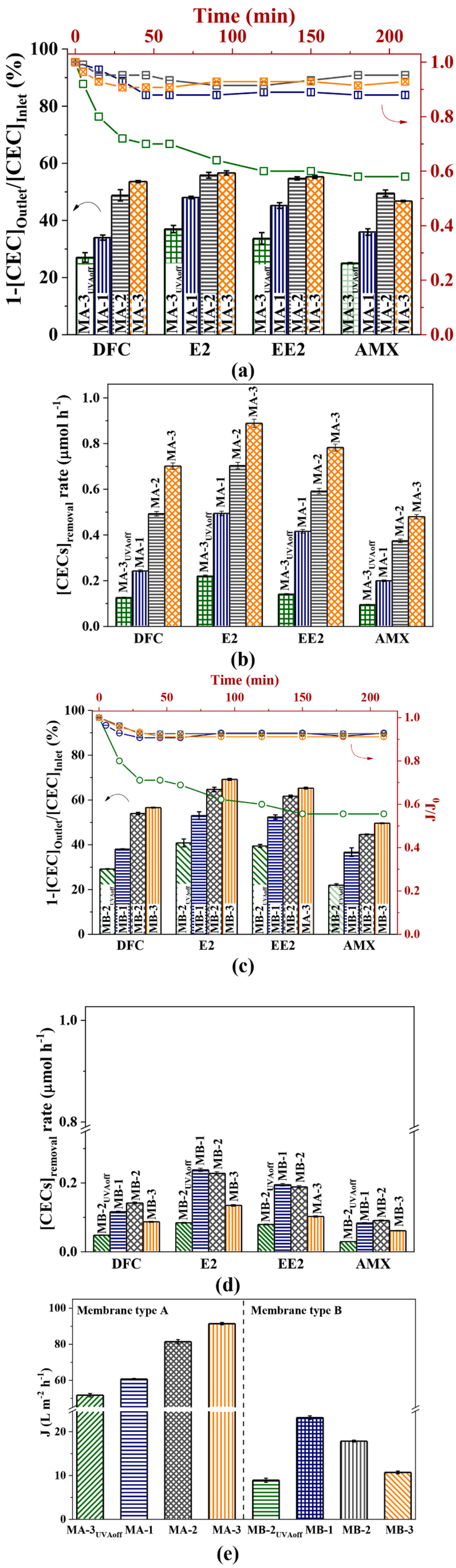

(caption on next column)

Fig. 4. CECs removal efficiency (a) and removal rate in µmol h^{-1} (b) from an UPW and, permeate flux as a function of the reaction time for the different catalyst films using membrane type A: MA-3$_{UVAoff}$ (▦; —□—), MA-1 (▥; —□—), MA-2 (▤; —□—) and, MA-3 (▩; —☒—); CECs removal efficiency (c) and removal rate in µmol h^{-1} (d) from an UPW and, permeate flux as a function of the reaction time for the different catalyst films using membrane type B: MB-2$_{UVAoff}$ (▧; —○—), MB-1 (▤; —⊖—), MB-2 (▩; —⊗—) and MB-3 (▥; —⦶—); e) Permeate flux in L m^{-2} h^{-1} after 210 min of reaction (J$_{210}$). Conditions: [CEC]$_0$ = 500 µg L^{-1}; T = 25 °C; CFV = 0.01 m s^{-1}; TMP = 10 bar.

3). The G band in thermally reduced TiO$_2$-sample slightly shifts to the lower frequencies, showing the broader peaks with higher intensities [44]. The intensity ratio ID/IG of the G sample (0.64) increased for the MA-3 sample (0.69) due to the removal of oxygenated groups after the thermal treatment (reestablishment of conjugated graphene network) [51]. The further analysis showed marginal G-band shrift (~5 cm^{-1}) to a lower frequency at 1589 cm^{-1} (from 1594 cm^{-1}), which confirms the interaction (charge transfer) between graphene and TiO$_2$ [39]. The broad 2D peak at 2960 cm^{-1} is typically present in the graphene spectra, indicating the possible formation of the multi-layer structure and the presence of the amorphous carbon phase [43,52].

The phase structures of the TiO$_2$-P25 samples after pyrolysis were confirmed by XRD and compared to pure TiO$_2$-P25, as shown in Fig. S2. The characteristic diffraction peaks appearing at 2θ = 25.3 and 2θ = 27.4 diffraction planes for the anatase and rutile, respectively [53] {Mani, 2012 #65}. The results before and after pyrolysis at 600 °C are similar. Kim et al. [54] reported that the anatase-rutile phase transformation occurred at temperatures above 600 °C. Therefore, the characterization data indicated that the heat treatment did not affect the TiO$_2$ crystallinity. Insert Fig. 3

3.2. *Performance of the photocatalytic membranes*

3.2.1. *Batch tests*

Preliminary CECs removal experiments using small pieces of the membranes were carried out in a batch reactor. All these experiments are laid out in Table S1. Experiments with a pristine membrane showed a negligible CECs removal, indicating insignificant i) photoactivity of the membrane material and ii) photolysis of CECs in the presence of UVA light. Furthermore, the membrane coated with TiO$_2$ and G-TiO$_2$ thin films showed negligible CECs adsorption.

However, the functionalized membranes boosted the CECs removal, where G-TiO$_2$ thin-films performed better than TiO$_2$ thin-film, indicating that the incorporation of TiO$_2$ nanoparticles on G nanosheets are able to improve the photocatalytic activity of the membrane surface. Membrane type B showed better results than membrane type A (maximum $k_{CEC\text{-}B}$ = 1.3-fold increase, #C11 and #D11) due to the better exposure of the TiO$_2$ nanoparticles to the UVA light. Although the increment in the amount of photocatalyst deposited on the membrane showed a positive effect on CECs oxidation, the reaction rate will reach a maximum value with further film thickness increase, as it will be discussed in the following sections [55].

3.2.2. *PMR tests using synthetic CECs solutions*

Prior to CEC oxidation experiments, the hydraulic permeability of each membrane was evaluated by the slope of the straight line obtained by plotting the water flux values, measured in fixed conditions of temperature (25 °C), as a function of the TMP (3, 5, 10 bar), according to Darcy's law (Fig. S3). The hydraulic permeability computed from the slope flux for MA-3 and MB-2 were 7.8 L m^{-2} h^{-1} bar^{-1} and 2.6 L m^{-2} h^{-1} bar^{-1}, respectively. The membrane hydrophilicity or wetting capacity is one of the most important factors for improving the pure water flux and reducing fouling. The membrane with less water-contact angle has better hydrophilicity properties [56]. The addition of TiO_2 nanoparticles on the membrane surface decreased the contact angle for MA-3 and reached a value of zero for MB-2 (Table S2). This can be attributed to the presence of TiO_2 hydrophilic nanoparticles in the upper layer of MB-2. The presence of TiO_2 nanoparticles containing a large number of hydrophilic hydroxyl groups on the surface of the membrane increases its hydrophilicity [57]. The outermost surface of membrane type B has a layer of TiO_2, which is highly wettable. However, below the layer of TiO_2, there is a layer of graphene that has hydrophobic characteristics. Although MB-2 has a smaller apparent contact angle than MA-3, the high TiO_2 content on the surface of membrane type B caused a high decrease in the permeate flux. This permeate flux decline could be attributed to pore blocking by the TiO_2 nanoparticles, correlated with the reduction in porosity and mean pore radius (see Fig. 1c and f).

In continuous-flow experiments using PMR, the pristine/commercial MF membrane could not reject CECs molecules due to its larger pore size when compared with the diameter of the target organic compounds and its non-photoactive characteristic. Furthermore, tests were carried out with the BPR fully open (no permeation) in the absence of light, in order to evaluate the possible adsorption of the CECs in the experimental setup. CECs adsorption on the membrane with and without a catalyst thin-film was negligible (<1%). However, in the presence of light and catalyst thin-film, CECs rejection achieved maximum values of nearly 60% (Fig. 4a and 4c). Insert Fig. 4

The membranes coated with multi-layer G-TiO_2 films (A or B) without physical treatment showed no water permeation (maximum pressure of 10 bar), confirming the hypothesis that the pores were created by the passage of an air stream through the membrane (inside-outside mode). This procedure creates nanogaps in the CS film after the catalyst deposition and before the pyrolysis step. The success of the pore preparation process in multi-layer graphene membrane derives from the ability of CS to form conformal, continuous films on arbitrary substrates and its subsequent transformation into defective doped G upon pyrolysis at 600 °C. Pyrolysis causes a profound structural change of the polysaccharide forming doped G even after physical treatment. The goal was to achieve a membrane able to reject CECs and allow the permeation of nutrients, producing a safe and nutrient-rich permeate for irrigation in agriculture [58]. For example, recent experimental investigations using a microfiltration membrane proved that physical opening methods using an electron beam or a laser could be an excellent approach to create variable-sized graphene nanopores to tune selectivity and molecular diffusivity [59].

As expected, in the presence of UVA light, the functionalized membranes exhibit an improvement in the membrane permeate flux and quality, and reduced membrane fouling (Fig. 4), due to the synergetic functions for CECs oxidation and self-cleaning process. Maximum CECs rejection coupling continuous filtration with photocatalysis were as follows: (i) 48 and 53% (DFC); (ii) 56 and 65% (E2); (iii) 54 and 62% (EE2); 49 and 45% (AMX) for membranes MA-3 and MB-2, respectively. Membrane type B enables a slightly higher CECs rejection than membrane type A, which can be explained mainly by the better exposure of the photocatalyst to light. As the preparation method of membrane type B only inserts TiO_2 after the formation of the G layer in the membrane shell-side, a greater amount of catalyst is susceptible to being activated by UVA light. For membrane type B, catalyst thin-films with approximately 17, 24 and 30 mg of TiO_2 were obtained when 3, 6 and 9 immersions of the G membrane in the catalyst suspension were carried out. Although an increment on the catalyst film thickness improved the CECs rejection efficiency, permeate flux declined (Fig. 4c, to be further discussed below), leading to a maximum CECs removal rate (μmol h^{-1}) (Fig. 4d) for the catalyst film with 6 layers.

For membrane type A, CECs removal efficiency (Fig. 4a), permeate flux (Fig. 4e) and consequently, CECs removal rate (Fig. 4b) increased with the increment on TiO_2 mass (1, 2 and 3% w/v) used in the preparation of the CS solution (before pyrolysis). For values higher than 4% w/v, the film was not continuous and for that reason, 3% w/v was considered the optimum concentration of TiO_2.

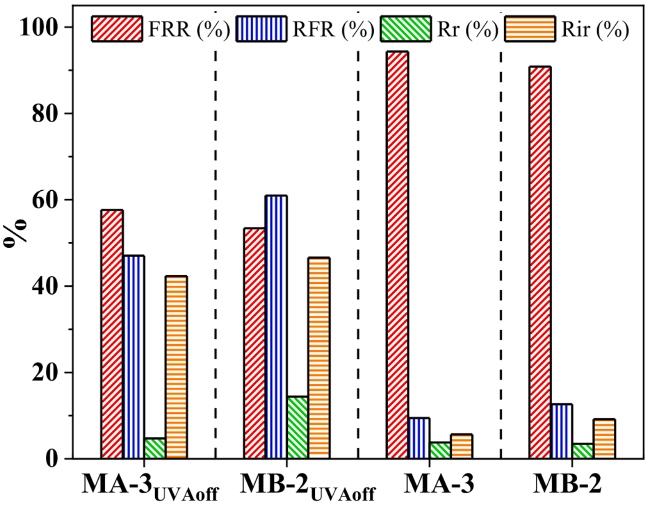

Fig. 5. Flux recovery ratio (FRR), relative flux reduction ratio (RFR), reversible fouling ratio (Rr) and irreversible fouling ratio (Rir) to assess antifouling performance of G-TiO_2 membranes with (MA-2 and MB-3) and without (MA-3$_{UVAoff}$ and MB-2$_{UVAoff}$) UVA irradiation.

According to the data presented in Fig. 4b and 4d, the CECs removal rate followed the sequence E2 > EE2 > DCF > AMX. CECs have starkly different chemical properties, and their particle size can vary from 11.5 to 46 μm (mean molecule size: DCF – 11.5–39.6 μm; AMX – 10–30 μm; E2/EE2 – 30–46 μm) [60–62]. Under the experimental conditions (pH = 6.9), DCF and AMX are both negatively charged molecules. Also, the pH_{pzc} for the G-TiO_2 film powder was found to be 6.4 (Fig. S4). As the solution pH is higher than the catalyst zero-point charge, the surface of G-TiO_2 film is negatively charged, providing selective rejection of the negatively charged CECs. These results were confirmed by the zeta potential analyses (Table S2). Regarding hormones, neutral molecules for the pH working conditions, their rejections positively correlated with their larger molecular dimension (size exclusion) and fairly hydrophobic characteristics ($\log K_{OW} = 4.01$ and $\log K_{OW} = 3.67$, respectively).

In the presence of light, the CECs rejection can be correlated with its reactivity towards hydroxyl radicals (E2 - $k_{\bullet OH} = (1.2 \pm 0.3) \times 10^{10}\ M^{-1}\ s^{-1}$; EE2 - $k_{\bullet OH} = (1.5 \pm 0.2) \times 10^{10}\ M^{-1}\ s^{-1}$); DCF - $k_{\bullet OH} = (9.29 \pm 0.11) \times 10^{9}\ M^{-1}\ s^{-1}$; AMX - $k_{\bullet OH} = (3.93\text{–}7.95) \times 10^{9}\ M^{-1}\ s^{-1}$) [63–66] and higher driving force for the catalyst surface ($[E2]_{feed} = 2.1 \pm 0.2$ mM > $[EE2]_{feed} = 1.8 \pm 0.1$ mM > $[DCF]_{feed} = 1.64 \pm 0.09$ mM > $[AMX]_{feed} = 1.29 \pm 0.08$ mM). During the usual membrane filtration process, solutes are transported from the surface of the membrane ($C_{surface}$) to the bulk cross-flow by convective transport ($J_{Convection}$) as a part of the permeate flow. Solutes that are rejected accumulate (C_{bulk}) near the surface forming either deposits or a gelatinous-type layer (fouling). This solute build-up will cause a steep concentration gradient within the boundary layer, causing a back-transport of solute into the bulk stream due to diffusion ($J_{diffusion}$) [67]. Consequently, there is an exponential increase in the concentration of organic compounds near the membrane surface (Fig. S5), which are oxidized by the action of reactive species, such as superoxide radicals ($O_2^{-\bullet}$), photogenerated holes (h^+), and hydroxyl radicals ($OH^\bullet$), generated when the G-TiO_2 film is exposed to light (UVA) [28]. Therefore, a hybrid system that couples membrane filtration and photocatalytic processes appear to be an alternative pathway to preclude the fouling and improve CECs removal.

In this study, the permeate flux changes were monitored for 210 min where the starting point of the reaction was carried out by permeation of UPW and the following points were accomplished with a CEC solution. The permeability performance of G-TiO_2 membranes was investigated

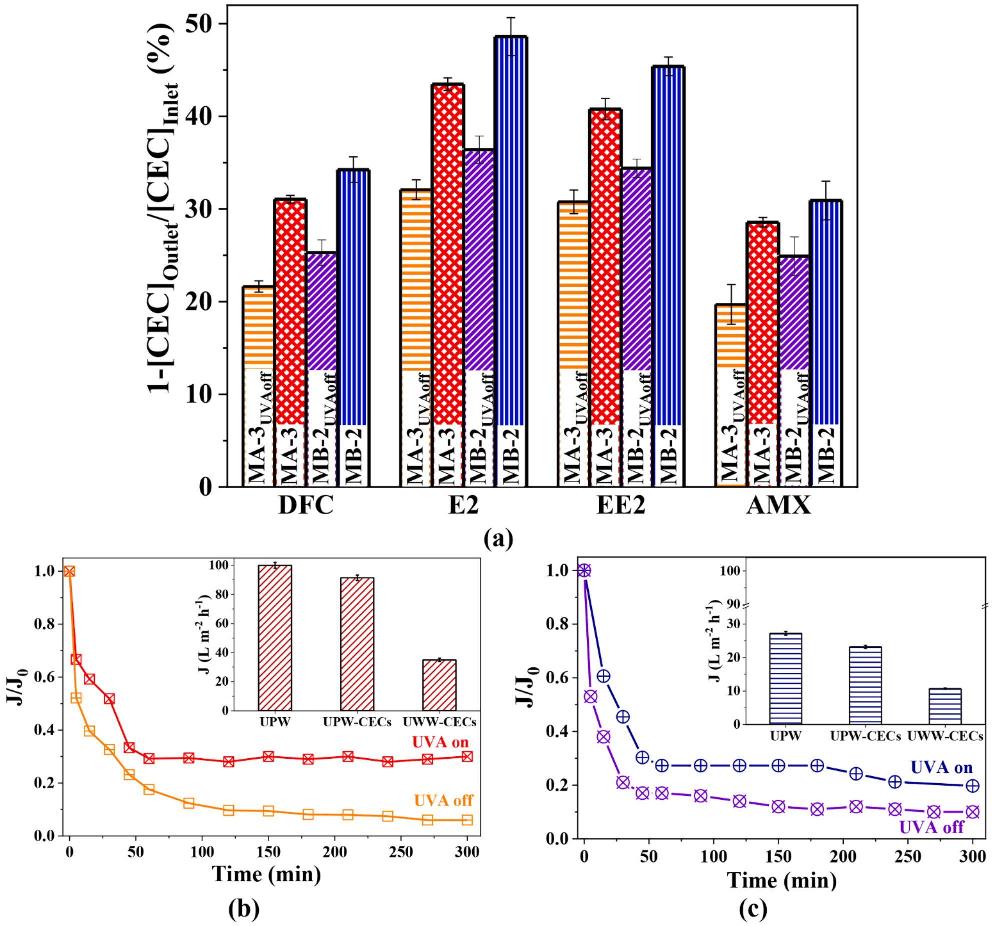

Fig. 6. a) CECs removal from an UWW and permeate flux as a function of the reaction time for the best catalyst conditions using membrane type A (b): MA-3_{UVAoff} (▤, –□–); MA-3 (▦, –☒–); and membrane type B (c): MB-2_{UVAoff} (▨, –⊗–), MB-2 (▥, –⊕–). Conditions: $[CEC]_0 = 500$ µg L^{-1}; T = 25 °C; pH = 6.7; CFV = 0.01 m s^{-1}; TMP = 10 bar.

and presented in Fig. 4a and 4c. As can be seen, the highest permeate flux decline was observed at the beginning of the experiments and after 30 min of reaction time, the permeate flux achieved steady-state conditions in the presence of UVA light (MA-1, MA-2, MA-3, MB-1, MB-2 and MB-3). In the absence of UVA light (MA-3_{UVAoff} and MB-2_{UVAoff}), the decline in the permeate flux was continuous and did not reach a steady-state condition even after 210 min of reaction. Generally, the reduction in permeate flow is attributed to the fouling phenomenon in which the size exclusion, hydrophobic interaction and electrostatic repulsion are the mechanisms responsible for the fouling of the membrane surface [68]. In the absence of UVA light, the RFR of MA-3 or MB-2 membranes decreased 40 and 45% owing to membrane fouling, respectively.

As shown in Fig. 5, the G-TiO_2-UVA system (MA-3 and MB-2) has a lower RFR and higher FRR than the G-TiO_2 system (MA-3_{UVAoff} and MB-2_{UVAoff}). Generally, lower RFR and higher FRR values indicate better antifouling properties of a membrane. Additionally, fouling can be divided into reversible (Rr) and irreversible (Rir) fouling. Rr is a fouling that could be cleaned by re-washing and is caused by the rejected contaminant molecules adsorbed or deposited on the surface of the membrane. Rir fouling is mainly removed by chemical washing or enzymatic degradation and is formed by various compounds that strongly bind with the membrane. Fig. 5 shows that both Rr and Rir fouling strongly decreased with the use of the G-TiO_2-UVA system. For example, Rir decreased from 42.3 and 46.6% for MA-3_{UVAoff} and MB-2_{UVAoff} to 5.7 and 9.2% for the MA-3 or MB-2, respectively. The G-TiO_2 membranes have not only a lower RFR value but also a lower Rir value, which indicates a higher longevity of the fabricated membranes. Similar results were also obtained by Xu et al. [69], using a PVDF ultrafiltration membranes based on the synergy of GO and TiO_2.

Hence, the G-TiO_2-UVA system presents a better permeability and antifouling properties when compared to the system in the absence of light. Fig. 4e also presents the permeate flux during filtration of CECs solution through the examined membranes. After 210 min, the permeate flux reached maximum values of 91 L m^{-2} h^{-1} and 23 L m^{-2} h^{-1} for the MA-3 and MB-2 membranes, respectively. Membrane type A shows the highest water permeability, which may be attributed to the pyrolysis of the CS with TiO_2 nanoparticles, resulting in more defects in the continuous G film. The results showed that the permeability of membrane type A increased according to the concentration of TiO_2 nanoparticles up to 3% ([w/v]), when the film started to create gaps in the continuous film. On the other hand, when the photocatalyst was added over the G film (membrane type B), there was a significant decrease in the permeate flux after 210 min (J_{210}) for increasing amounts of TiO_2 ($J_{210\text{-MB-1}} = 23$ L m^{-2} h^{-1}; $J_{210\text{-MB-2}} = 18$ L m^{-2} h^{-1}; $J_{210\text{-MB-3}} = 11$ L m^{-2} h^{-1}). Therefore, the accumulation of nanoparticles may lead to porosity reduction, which affects the flux through the membrane. Insert Fig. 5

The long-term stability of the G-TiO_2 nanocomposite thin-film was evaluated for an operation period of 12 h. The relative permeates flux (J_{CECs}/J_0) of the membranes A and B with/without UVA radiation (MA-3_{UVAoff}, MB-2_{UVAoff}, MA-3 and MB-2) versus time is displayed in Fig. S6. The obtained results reveal that a considerable flux decline for all membranes is observed during the first min of operation. However, after 60 min of filtration the membranes with UVA radiation reached an almost constant flux, and the membranes without UVA radiation had a steep slope up to approximately 60% with 300 min. Moreover, although all the membranes showed a flux decline during the filtration process, at the end of the 12-hour filtration, MA-3 and MB-2 membranes reveal about 40 and 50% higher permeate flux than the respective membranes without UVA radiation, suggesting the superior potential of membranes with catalyst activation. The stability of catalyst films was also evaluated based on the CECs removal for a period of 12 h. Fig. S6b shows the treatment level achieved for each CEC throughout the experiment. In general, the CECs removal percentage level was stable throughout the monitored period, with no evident trends of decreased treatment performance. Mean levels of treatment ranged from 45% removal of AMX to 65% removal of E2 for the G-TiO_2-UVA systems.

3.2.3. PMR tests using UWW matrix fortified with CECs

The effectiveness of the PMR system, using MA-3 and MB-2 membranes, was evaluated towards CECs removal from a secondary effluent from an urban WWTP fortified with 500 μg L^{-1} of each CEC (Fig. 6). Fig. 6b and 6c show high RFR values of 70–75%, using the UWW matrix, near 12 times higher than when using synthetic CECs solutions. This is associated with the presence of organic matter in the UWW, resulting in the formation of a dense cake layer around the membrane shell-side, contributing to a rapid deterioration of the permeate flux. UWW components include a broad range of organic (e.g., natural organic matter composed of humic and fulvic acids, carbohydrates, proteins) and inorganic species (e.g., carbonate, bicarbonate, nitrite, sulphate, chloride), which react with $OH^{\bullet}$ and $O_2^{-\bullet}$ radicals, either competing with organic CECs for oxidation or forming the respective radicals with lower oxidation potential [70,71]. Moreover, the presence of cation ions (Ca^{2+}, Mg^{2+} and K^{+}) in the UWW solutions (Table 2), might led to a less negative G-TiO_2 membrane surface due to charge shielding and chemical adsorption [72]. As expected, in the presence of the UVA light, pollutants are oxidized on the membrane surface, showing a lower decline in the permeate flux when compared with the system in the absence of UVA light (RFR higher than 90%) (Fig. 6b and 6c). Regarding the permeate flux, as observed during the filtration of a pure synthetic CECs solution, MA-3 presents higher values than MB-2 (inset graphics of Fig. 6b and 6c).

Although the UWW matrix affects the permeate flux negatively, CECs rejection was not significantly affected, achieving maximum values of: (i) 31 and 34% (DFC); (ii) 43 and 49% (E2); (iii) 41 and 45% (EE2); and 29 and 31% (AMX), respectively for MA-3 and MB-2 membranes irradiated by UVA light (Fig. 6a). The decline in CECs rejection can be associated with: i) the existing contaminants (organic and inorganic matter) in the UWW matrix that are capable of inhibiting the rate of CECs removal, ii) the deposited/adsorbed pollutants onto the catalyst's film, preventing the catalyst contact with light, oxygen and water, negatively affecting the photocatalytic activity.

As in the CECs synthetic solution studies, MB-2 behaves better than MA-3, considering the CECs removal. The well-controlled morphology (the pore exposure/accessibility, the functionality/hydrophilicity of the surface), efficient TiO_2 interactions with the graphene and good material stability disclose the role of multicomponent hybrid photocatalytic-membrane system. Insert Fig. 6

3.3. *Toxicity*

The zebrafish embryo bioassays met the OECD FET test 236 criteria: overall survival and hatching rate in control and solvent control at the end of the 96 h exposure were ≥ 90% and 80%, respectively. Moreover, no significant differences were observed between control and solvent control.

Mortality, total abnormalities, and hatching rate observed on zebrafish embryos exposed to the CECs in synthetic or real matrices before and after the treatment using MA-3 or MB-2 are presented in Table 3. A significant increase of total abnormalities (sum of pericardial

Table 3
Toxicological effects observed in zebrafish embryos exposed to the CECs, in synthetic and real matrices (dechlorinated water and UWWTP secondary effluent, respectively) before and after the treatment with the ceramic membranes MA-3 and MB-2.

Hours post fertilization (hpf)	Treatment	Endpoints		
		Mortality (%)	Total abnormalities (%)	Hatching (%)
24	Synthetic matrix (dechlorinated water - control)	2.1 ± 0.6	0 ± 0	0 ± 0
	Synthetic matrix + acetonitrile (sol. control)	5 ± 5	0 ± 0	0 ± 0
	Synthetic matrix + CECs	15 ± 6 *	0 ± 0	0 ± 0
	Synthetic matrix + CECs + MA-3	10 ± 6	0 ± 0	0 ± 0
	Synthetic matrix + CECs + MB-2	5 ± 5	0 ± 0	0 ± 0
	Real matrix (UWWTP secondary effluent)	5 ± 5	0 ± 0	0 ± 0
	Real matrix + acetonitrile	5 ± 5	0 ± 0	0 ± 0
	Real matrix + CECs	5 ± 5	10 ± 6	0 ± 0
	Real matrix + CECs + MA-3	5 ± 5	0 ± 0	0 ± 0
	Real matrix + CECs + MB-2	5 ± 5	0 ± 0	0 ± 0
48	Synthetic matrix (dechlorinated water - control)	2.1 ± 0.6	0 ± 0	0 ± 0
	Synthetic matrix + acetonitrile (sol. control)	5 ± 5	0 ± 0	0 ± 0
	Synthetic matrix + CECs	15 ± 6 *	7 ± 7	0 ± 0
	Synthetic matrix + CECs + MA-3	10 ± 6	5 ± 5	0 ± 0
	Synthetic matrix + CECs + MB-2	5 ± 5	0 ± 0	0 ± 0
	Real matrix (UWWTP secondary effluent)	5 ± 5	0 ± 0	0 ± 0
	Real matrix + acetonitrile	5 ± 5	0 ± 0	0 ± 0
	Real matrix + CECs	5 ± 5	100 ± 0 * # &	0 ± 0
	Real matrix + CECs + MA-3	5 ± 5	0 ± 0	0 ± 0
	Real matrix + CECs + MB-2	5 ± 5	0 ± 0	0 ± 0
72	Synthetic matrix (dechlorinated water - control)	2.1 ± 0.6	0 ± 0	17 ± 2
	Synthetic matrix + acetonitrile (sol. control)	5 ± 5	0 ± 0	$(3 \pm 1) \times 10^1$
	Synthetic matrix + CECs	15 ± 6 *	27 ± 2 * # &	0 ± 0 #
	Synthetic matrix + CECs + MA-3	10 ± 6	0 ± 0	$(4 \pm 1) \times 10^1$
		5 ± 5	5 ± 5	10 ± 6

(continued on next page)

Table 3 (*continued*)

Hours post fertilization (hpf)	Treatment	Endpoints		
		Mortality (%)	Total abnormalities (%)	Hatching (%)
	Synthetic matrix + CECs + MB-2			
	Real matrix (UWWTP secondary effluent)	5 ± 5	5 ± 5	$(6 \pm 2) \times 10^1$
	Real matrix + acetonitrile	5 ± 5	0 ± 0	$(4 \pm 1) \times 10^1$
	Real matrix + CECs	$(4 \pm 1) \times 10^1$ * # &	100 ± 0 * # &	0 ± 0 *
	Real matrix + CECs + MA-3	5 ± 5	0 ± 0	$(2 \pm 1) \times 10^1$
	Real matrix + CECs + MB-2	5 ± 5	5 ± 5	10 ± 6
96	Synthetic matrix (dechlorinated water - control)	2.1 ± 0.6	2.1 ± 0.6	97.9 ± 0.6
	Synthetic matrix + acetonitrile (sol. control)	5 ± 5	10 ± 6	95 ± 5
	Synthetic matrix + CECs	20 ± 5 * &	88 ± 7 * # &	10 ± 6 * # &
	Synthetic matrix + CECs + MA-3	10 ± 6	5 ± 5	90 ± 6
	Synthetic matrix + CECs + MB-2	5 ± 5	5 ± 5	95 ± 5
	Real matrix (UWWTP secondary effluent)	5 ± 5	5 ± 5	95 ± 5
	Real matrix + acetonitrile	5 ± 5	5 ± 5	95 ± 5
	Real matrix + CECs	100 ± 0 * # &	A	A
	Real matrix + CECs + MA-3	5 ± 5	0 ± 0	100 ± 0
	Real matrix + CECs + MB-2	5 ± 5	5 ± 5	80 ± 9

"*" indicates significant differences ($p < 0.05$) between CECs in synthetic or in real matrix and control or UWWTP; "#" and "&" indicate significant differences between treated and non-treated groups (i.e., CECs in synthetic or real matrices before and after the treatments with the MA-3 and MB-2, respectively); a – not measured because all embryos died. Data are expressed as mean ± SE (N = 10 for control; N = 5 for the other treatments).

and yolk-sac oedemas and notochord malformation) was observed in embryos exposed to the CECs plus synthetic or real matrices when compared with both matrices without CECs. After 48 h of exposure to CECs in the real matrix, 100% of the embryos showed pericardial and yolk sac oedemas, and abnormalities in the notochord (Table 3, Fig. 7) compared with 5% abnormalities in the real matrix. At 72 and 96 h, 35 and 100% of embryos died, respectively, in the real matrix with CECs. Similarly, although less severe, the embryos exposed to CECs in the synthetic matrix also presented a significant increase of abnormalities (88.3%) at 96 h (Table 3, Fig. 7) compared with no abnormalities recorded at the synthetic matrix alone at this time point. The mortality rate for the CECs plus synthetic matrix reached 15% at 72 h and 20% at 96 h compared to 2.1% in synthetic matrix alone in these time points. With regard to the hatching rate, no embryos hatched after exposition to CECs in the real matrix and all of them died at 96 h. The hatching rate for the embryos exposed to CECs in the synthetic matrix was significantly reduced at 96 h with only 10% of the embryos hatched, compared to 97.9% in the synthetic matrix alone.

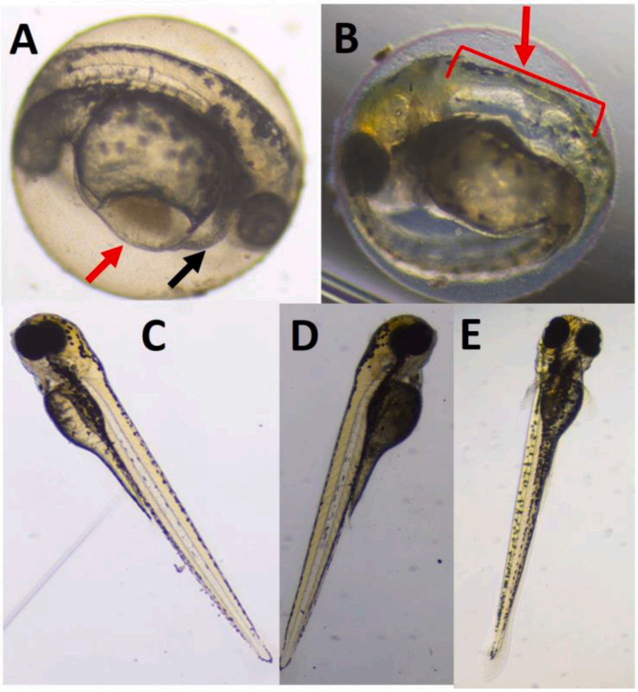

Fig. 7. Abnormalities observed in the zebrafish embryo bioassay: Pericardial oedema – black arrow; yolk sac oedema – red arrow at 48 hpf exposition to CECs + real matrix (A); Abnormal notochord formation at 96 hpf exposition to CECs + synthetic matrix (B); normal development at 96 hpf recorded in CECs + real matrix + MA-3 (C), CECs + real matrix + MB-2 (D) and control – synthetic water (E).

The abnormalities and mortality reported for the CECs in both matrices were significantly reduced after the treatment using MA-3 or MB-2 with values similar to the synthetic and real matrices ($p > 0.05$) (Table 3, Fig. 7). The same effect was observed for the endpoint hatching rate that was significantly increased after the treatment using both types of membranes. It is evident that the filtration + oxidation treatment process increased the fitness of zebrafish embryos and led to a significant decrease in the toxicity produced by CECs present in the synthetic and real matrices. Insert Table 3 Insert Fig. 7

4. Conclusions

The PMR with the functionalized membranes, activated by UVA light, operated in a single-pass flow-through mode for the treatment of synthetic CECs solutions, exhibits a substantial improvement in the membrane permeate quality and quantity compared to its performance in the absence of light. The G-TiO_2-UVA systems present high stability for at least 12 h of continuous operation and reduced reversible and irreversible fouling due to the synergetic functions for CECs oxidation and self-cleaning process. Overall, the results in this study indicate that the G-TiO_2-UVA systems investigated achieve good removal of CECs and were able to reduce CECs toxicity to zebrafish embryos effectively. Membrane type B enables a slightly higher CECs rejection than membrane type A, which can be explained mainly by its better exposure of the photocatalyst to light. However, the accumulation of the nanoparticles over the G film increases the surface roughness of membrane MB-2, confirmed by AFM analysis, reducing its resistance to fouling when to compared to membrane MA-3.

Although the UWW matrix showed a significant negative effect on permeate flux when compared to UPW, mainly due to the presence of substances that may deposit or adsorb onto the membrane's surface (blocking the membrane pores), the CECs rejection was similar to the one obtained with UPW.

Declaration of Competing Interest

The authors declare that they have no known competing financial interests or personal relationships that could have appeared to influence the work reported in this paper.

Acknowledgments

This work was financially supported by: i) Project NOR-WATER funded by INTERREG VA Spain-Portugal cooperation programme, Cross-Border North Portugal/Galizia Spain Cooperation Program (POCTEP); ii) Project SERPIC funded by the European Unionś Horizon 2020 research and innovation programme under grant agreement No. 869178-AquaticPollutants; and iii) Base-UIDB/50020/2020 and Programmatic-UIDP/50020/2020 Funding of LSRE-LCM, funded by national funds through FCT/MCTES (PIDDAC). P. H. Presumido acknowledges FCT for his scholarship (SFRH/BD/138756/2018). Vítor J. P. Vilar acknowledges the FCT Individual Call to Scientific Employment Stimulus 2017 (CEECIND/01317/2017). Maja Đolić acknowledges the grants issued from the Ministry of Education and Science of the Republic of Serbia (Contract No. 451-03-9/2021-14/200135). We also thank Amparo Forneli for assistance in characterizing G-TiO_2 films. Financial support by the Spanish Ministry of Science and Innovation (Severo Ochoa and RTI2018-890237-CO_2-R1) and Generalitat Valenciana (Prometeo 2017-83) is also gratefully acknowledged.

Appendix A. Supplementary data

Supplementary data to this article can be found online at https://doi.org/10.1016/j.cej.2021.132639.

References

[1] J.P. Meador, A. Yeh, G. Young, E.P. Gallagher, Contaminants of emerging concern in a large temperate estuary, Environ. Pollut. 213 (2016) 254–267, https://doi.org/10.1016/j.envpol.2016.01.088.

[2] European Commission, Regulation (EU) 2020/741 of the European Parliament and of the Council of 25 May 2020 on minimum requirements for water reuse, Off. J. Eur. Comm. L 177/32 (2020).

[3] P. Vergine, S. Amalfitano, C. Salerno, G. Berardi, A. Pollice, Reuse of ultrafiltered effluents for crop irrigation: On-site flow cytometry unveiled microbial removal patterns across a full-scale tertiary treatment, Sci. Total. Environ. 718 (2020) 1–9, https://doi.org/10.1016/j.scitotenv.2020.137298.

[4] P. Vergine, C. Salerno, A. Libutti, L. Beneduce, G. Gatta, G. Berardi, A. Pollice, Closing the water cycle in the agro-industrial sector by reusing treated wastewater for irrigation, J. Clean. Prod. 164 (2017) 587–596, https://doi.org/10.1016/j.jclepro.2017.06.239.

[5] S. Bunani, E. Yörükoğlu, Ü. Yüksel, N. Kabay, M. Yüksel, G. Sert, Application of reverse osmosis for reuse of secondary treated urban wastewater in agricultural irrigation, Desalination 364 (2015) 68–74, https://doi.org/10.1016/j.desal.2014.07.030.

[6] T. Sun, Y. Liu, L. Shen, Y. Xu, R. Li, L. Huang, H. Lin, Magnetic field assisted arrangement of photocatalytic TiO_2 particles on membrane surface to enhance membrane antifouling performance for water treatment, J. Colloid. Interf. Sci. 570 (2020) 273–285, https://doi.org/10.1016/j.jcis.2020.03.008.

[7] J. Teng, Y. Chen, G. Ma, H. Hong, T. Sun, B.-Q. Liao, H. Lin, Membrane fouling by alginate in polyaluminum chloride (PACl) coagulation/microfiltration process: Molecular insights, Sep. Purif. Technol. 236 (2020) 1–10, https://doi.org/10.1016/j.seppur.2019.116294.

[8] J.C. Espíndola, R.O. Cristóvão, A. Mendes, R.A.R. Boaventura, V.J.P. Vilar, Photocatalytic membrane reactor performance towards oxytetracycline removal from synthetic and real matrices: Suspended vs immobilized TiO_2-P25, Chem. Eng. J. 378 (2019), 122114, https://doi.org/10.1016/j.cej.2019.122114.

[9] Y. Shi, J. Huang, G. Zeng, W. Cheng, J. Hu, Photocatalytic membrane in water purification: is it stepping closer to be driven by visible light? J. Membrane Sci. 584 (2019) 364–392, https://doi.org/10.1016/j.memsci.2019.04.078.

[10] O.K. Dalrymple, D.H. Yeh, M.A. Trotz, Removing pharmaceuticals and endocrine-disrupting compounds from wastewater by photocatalysis, J. Chem. Technol. Biot. 82 (2) (2007) 121–134, https://doi.org/10.1002/jctb.1657.

[11] D. Kanakaraju, B.D. Glass, M. Oelgemöller, Advanced oxidation process-mediated removal of pharmaceuticals from water: A review, J. Environ. Manage. 219 (2018) 189–207, https://doi.org/10.1016/j.jenvman.2018.04.103.

[12] W. Zhang, L. Ding, J. Luo, M.Y. Jaffrin, B. Tang, Membrane fouling in photocatalytic membrane reactors (PMRs) for water and wastewater treatment: A critical review, Chem. Eng. J. 302 (2016) 446–458, https://doi.org/10.1016/j.cej.2016.05.071.

[13] X. Zhang, T. Zhang, J. Ng, D.D. Sun, High-Performance Multifunctional TiO_2 Nanowire Ultrafiltration Membrane with a Hierarchical Layer Structure for Water Treatment, Adv. Funct. Mater. 19 (23) (2009) 3731–3736, https://doi.org/10.1002/adfm.200901435.

[14] R. Qian, H. Zong, J. Schneider, G. Zhou, T. Zhao, Y. Li, J. Yang, D.W. Bahnemann, J.H. Pan, Charge carrier trapping, recombination and transfer during TiO_2 photocatalysis: An overview, Catal. Today 335 (2019) 78–90, https://doi.org/10.1016/j.cattod.2018.10.053.

[15] A.M. Chávez, R.R. Solís, F.J. Beltrán, Magnetic graphene TiO_2-based photocatalyst for the removal of pollutants of emerging concern in water by simulated sunlight aided photocatalytic ozonation, Appl. Catal. B-Environ. 262 (2020), 118275, https://doi.org/10.1016/j.apcatb.2019.118275.

[16] L. Yang, L. Xu, X. Bai, P. Jin, Enhanced visible-light activation of persulfate by Ti^{3+} self-doped TiO_2/graphene nanocomposite for the rapid and efficient degradation of micropollutants in water, J. Hazard. Mater. 365 (2019) 107–117, https://doi.org/10.1016/j.jhazmat.2018.10.090.

[17] Z. Zhou, Z. Shen, Z. Cheng, G. Zhang, M. Li, Y. Li, S. Zhan, J.C. Crittenden, Mechanistic insights for efficient inactivation of antibiotic resistance genes: a synergistic interfacial adsorption and photocatalytic-oxidation process, Sci. Bull. 65 (24) (2020) 2107–2119, https://doi.org/10.1016/j.scib.2020.07.015.

[18] N.A. Almeida, P.M. Martins, S. Teixeira, J.A. Lopes da Silva, V. Sencadas, K. Kühn, G. Cuniberti, S. Lanceros-Mendez, P.A.A.P. Marques, TiO_2/graphene oxide immobilized in P(VDF-TrFE) electrospun membranes with enhanced visible-light-induced photocatalytic performance, J. Mater. Sci. 51 (14) (2016) 6974–6986, https://doi.org/10.1007/s10853-016-9986-4.

[19] G. Rao, Q. Zhang, H. Zhao, J. Chen, Y. Li, Novel titanium dioxide/iron (III) oxide/graphene oxide photocatalytic membrane for enhanced humic acid removal from water, Chem. Eng. J. 302 (2016) 633–640, https://doi.org/10.1016/j.cej.2016.05.095.

[20] M. Bojarska, B. Nowak, J. Skowroński, W. Piątkiewicz, L. Gradoń, Growth of ZnO nanowires on polypropylene membrane surface—Characterization and reactivity, Appl. Surf. Sci. 391 (2017) 457–467, https://doi.org/10.1016/j.apsusc.2016.04.130.

[21] S. Yu, Y. Wang, F. Sun, R. Wang, Y. Zhou, Novel mpg-C_3N_4/TiO_2 nanocomposite photocatalytic membrane reactor for sulfamethoxazole photodegradation, Chem. Eng. J. 337 (2018) 183–192, https://doi.org/10.1016/j.cej.2017.12.093.

[22] S. Liang, K. Xiao, Y. Mo, X. Huang, A novel ZnO nanoparticle blended polyvinylidene fluoride membrane for anti-irreversible fouling, J. Membrane Sci. 394–395 (2012) 184–192, https://doi.org/10.1016/j.memsci.2011.12.040.

[23] J. Zhang, Q. Xue, X. Pan, Y. Jin, W. Lu, D. Ding, Q. Guo, Graphene oxide/polyacrylonitrile fiber hierarchical-structured membrane for ultra-fast microfiltration of oil-water emulsion, Chem. Eng. J. 307 (2017) 643–649, https://doi.org/10.1016/j.cej.2016.08.124.

[24] C.P. Athanasekou, S. Morales-Torres, V. Likodimos, G.E. Romanos, L.M. Pastrana-Martinez, P. Falaras, D.D. Dionysiou, J.L. Faria, J.L. Figueiredo, A.M.T. Silva, Prototype composite membranes of partially reduced graphene oxide/TiO_2 for photocatalytic ultrafiltration water treatment under visible light, Appl. Catal. B-Environ. 158–159 (2014) 361–372, https://doi.org/10.1016/j.apcatb.2014.04.012.

[25] C.P. Athanasekou, N.G. Moustakas, S. Morales-Torres, L.M. Pastrana-Martínez, J. L. Figueiredo, J.L. Faria, A.M.T. Silva, J.M. Dona-Rodriguez, G.E. Romanos, P. Falaras, Ceramic photocatalytic membranes for water filtration under UV and visible light, Appl. Catal. B-Environ. 178 (2015) 12–19, https://doi.org/10.1016/j.apcatb.2014.11.021.

[26] W. Li, J. Li, N. Wang, X. Li, Y. Zhang, Q. Ye, S. Ji, Q.-F. An, Recovery of bio-butanol from aqueous solution with ZIF-8 modified graphene oxide composite membrane, J. Membrane Sci. 598 (2020), 117671, https://doi.org/10.1016/j.memsci.2019.117671.

[27] Y. Gao, M. Hu, B. Mi, Membrane surface modification with TiO_2–graphene oxide for enhanced photocatalytic performance, J. Membrane Sci. 455 (2014) 349–356, https://doi.org/10.1016/j.memsci.2014.01.011.

[28] P. Gao, Z. Liu, M. Tai, D.D. Sun, W. Ng, Multifunctional graphene oxide–TiO_2 microsphere hierarchical membrane for clean water production, Appl. Catal. B-Environ. 138–139 (2013) 17–25, https://doi.org/10.1016/j.apcatb.2013.01.014.

[29] S.G.S. Santos, L.O. Paulista, T.F.C.V. Silva, M.M. Dias, J.C.B. Lopes, R.A. R. Boaventura, V.J.P. Vilar, Intensifying heterogeneous TiO_2 photocatalysis for bromate reduction using the NETmix photoreactor, Sci. Total. Environ. 664 (2019) 805–816, https://doi.org/10.1016/j.scitotenv.2019.02.045.

[30] P.H. Presumido, A. Primo, V.J.P. Vilar, H. Garcia, Large area continuous multi-layer graphene membrane for water desalination, Chem. Eng. J. (2020), 127510, https://doi.org/10.1016/j.cej.2020.127510.

[31] A.M. Primo Arnau, H. García Gómez, E. Sánchez Cortezón, J.M. Delgado Sánchez, Method for obtaining solid graphene samples or suspensions, European Patent, Office (2015) 1–15.

[32] M.A. Ferro-García, J. Rivera-Utrilla, I. Bautista-Toledo, C. Moreno-Castilla, Adsorption of Humic Substances on Activated Carbon from Aqueous Solutions and Their Effect on the Removal of Cr(III) Ions, Langmuir 14 (7) (1998) 1880–1886, https://doi.org/10.1021/la970565h.

[33] M. Shakak, R. Rezaee, A. Maleki, A. Jafari, M. Safari, B. Shahmoradi, H. Daraei, S.-M. Lee, Synthesis and characterization of nanocomposite ultrafiltration membrane (PSF/PVP/SiO_2) and performance evaluation for the removal of amoxicillin from aqueous solutions, Environ. Technol. Innov. 17 (2020), 100529, https://doi.org/10.1016/j.eti.2019.100529.

[34] E.S. Galbavy, K. Ram, C. Anastasio, 2-Nitrobenzaldehyde as a chemical actinometer for solution and ice photochemistry, J. Photoch. Photobio. A 209 (2) (2010) 186–192, https://doi.org/10.1016/j.jphotochem.2009.11.013.

[35] American Public Health Association, Standard methods for the examination of water and wastewater, 19th ed., American Public Health Association, Washington, D.C., 1995.

[36] OECD, Test No. 236: Fish Embryo Acute Toxicity (FET) Test, OECD Guidelines for the Testing of Chemicals, Section 2, OECD Publishing, Paris, 2013. https://doi.org/doi:https://doi.org/10.1787/9789264203709-en.

[37] S. Barros, R. Montes, J.B. Quintana, R. Rodil, A. André, A. Capitão, J. Soares, M. M. Santos, T. Neuparth, Chronic environmentally relevant levels of simvastatin disrupt embryonic development, biochemical and molecular responses in zebrafish Danio rerio, Aquatic Toxicology 201 (2018) 47–57, https://doi.org/10.1016/j.aquatox.2018.05.014.

[38] J.C. Espíndola, R.O. Cristóvão, S.R.F. Araújo, T. Neuparth, M.M. Santos, R. Montes, J.B. Quintana, R. Rodil, R.A.R. Boaventura, V.J.P. Vilar, An innovative photoreactor, FluHelik, to promote UVC/H2O2 photochemical reactions: Tertiary treatment of an urban wastewater, Sci. Total Environ. 667 (2019) 197–207, https://doi.org/10.1016/j.scitotenv.2019.02.335.

[39] E.H. Alsharaeh, T. Bora, A. Soliman, F. Ahmed, G. Bharath, M.G. Ghoniem, K. M. Abu-Salah, J. Dutta, Sol-Gel-assisted microwave-derived synthesis of Anatase Ag/TiO_2/GO Nanohybrids toward efficient visible light phenol degradation, Catalysts 7 (5) (2017) 1–10, https://doi.org/10.3390/catal7050133.

[40] P. Benjwal, M. Kumar, P. Chamoli, K.K. Kar, Enhanced photocatalytic degradation of methylene blue and adsorption of arsenic(iii) by reduced graphene oxide (rGO)–metal oxide (TiO2/Fe3O4) based nanocomposites, RSC Adv. 5 (89) (2015) 73249–73260, https://doi.org/10.1039/C5RA13689J.

[41] P.T. Tuoi, N.N. Anh, B.H. Thang, P.V. Trinh, C.T. Thanh, D.N. Minh, N.V. Hung, N. V. Chuc, N.C. Khang, P.N. Minh, P.N. Hong, Optical and photocatalytic property of nanocomposite based functionalized graphene and TiO_2, The 8th International Workshop on Advanced Materials Science and Nanotechnology (IWAMSN2016), Vietnam, Ha Long City, 2016, pp. 398–404.

[42] N.R. Khalid, E. Ahmed, Z. Hong, Y. Zhang, M. Ahmad, Nitrogen doped TiO_2 nanoparticles decorated on graphene sheets for photocatalysis applications, Curr. Appl. Phys. 12 (6) (2012) 1485–1492, https://doi.org/10.1016/j.cap.2012.04.019.

[43] W. Zhou, Y. Liu, Y. Zhang, G. Yang, S. Deng, F. Shen, H. Peng, L. Wang, Novel multi-layer cross-linked TiO_2/C nanosheets and their photocatalytic properties, New J. Chem. 38 (4) (2014) 1647–1654, https://doi.org/10.1039/C3NJ01342A.

[44] M. Naebe, J. Wang, A. Amini, H. Khayyam, N. Hameed, L.H. Li, Y. Chen, B. Fox, Mechanical property and structure of covalent functionalized graphene/epoxy nanocomposites, Sci. Rep. 4 (1) (2014) 4375, https://doi.org/10.1038/srep04375.

[45] C.H. Manoratne, S.R.D. Rosa, I.R.M. Kottegoda, XRD-HTA, UV visible, FTIR and SEM interpretation of reduced graphene oxide synthesized from high purity vein graphite, Mater. Sci. Res. India 14 (1) (2017) 19–30, https://doi.org/10.13005/msri/140104.

[46] Z. Çiplak, N. Yildiz, A. Çalimli, Investigation of graphene/ag nanocomposites synthesis parameters for two different synthesis methods, Fuller. Nanotub. Car. N. 23 (4) (2015) 361–370, https://doi.org/10.1080/1536383X.2014.894025.

[47] Z. Xu, H. Gao, H. Guoxin, Solution-based synthesis and characterization of a silver nanoparticle–graphene hybrid film, Carbon 49 (14) (2011) 4731–4738, https://doi.org/10.1016/j.carbon.2011.06.078.

[48] V. Koutu, R. Dhakar, P. Ojha, L. Shastri, M.M. Malik, Structural and optical studies of TiO_2:Ag_2O nanocomposite by sol-gel method, Mater. Sci. Poland 38 (2) (2020) 263–270, https://doi.org/10.2478/msp-2020-0036.

[49] R. López, R. Gómez, Band-gap energy estimation from diffuse reflectance measurements on sol–gel and commercial TiO2: a comparative study, J. Sol-Gel Sci. Technol. 61 (1) (2012) 1–7, https://doi.org/10.1007/s10971-011-2582-9.

[50] Y. Wang, J. Yu, W. Xiao, Q. Li, Microwave-assisted hydrothermal synthesis of graphene based Au–TiO_2 photocatalysts for efficient visible-light hydrogen production, J. Mater. Chem. A 2 (11) (2014) 3847–3855, https://doi.org/10.1039/C3TA14908K.

[51] K.H. Leong, L.C. Sim, D. Bahnemann, M. Jang, S. Ibrahim, P. Saravanan, Reduced graphene oxide and Ag wrapped TiO_2 photocatalyst for enhanced visible light photocatalysis, Apl. Mater. 3 (10) (2015), 104503, https://doi.org/10.1063/1.4926454.

[52] I. Childres, L.A. Jauregui, W. Park, H. Cao, Y.P. Chen, Raman spectroscopy of graphene and related materials, in: J.I. Jang (Ed.), New Developments in Photon and Materials Research, Nova Science, New York, 2013, pp. 1–20.

[53] J. Mani, H. Sakeek, S. Habouti, M. Dietze, M. Es-Souni, Macro–meso-porous TiO2, ZnO and ZnO–TiO2-composite thick films Properties and application to photocatalysis, Catal. Sci. Technol. 2 (2) (2012) 379–385, https://doi.org/10.1039/C1CY00302J.

[54] D.J. Kim, S.H. Hahn, S.H. Oh, E.J. Kim, Influence of calcination temperature on structural and optical properties of TiO2 thin films prepared by sol–gel dip coating, Mater. Letters 57 (2) (2002) 355–360, https://doi.org/10.1016/S0167-577X(02)00790-5.

[55] D. Chen, F. Li, A.K. Ray, External and internal mass transfer effect on photocatalytic degradation, Catal. Today 66 (2) (2001) 475–485, https://doi.org/10.1016/S0920-5861(01)00256-5.

[56] Y. Zhang, F. Liu, Y. Lu, L. Zhao, L. Song, Investigation of phosphorylated TiO2–SiO2 particles/polysulfone composite membrane for wastewater treatment, Desalination 324 (2013) 118–126, https://doi.org/10.1016/j.desal.2013.06.007.

[57] M. Safarpour, A. Khataee, V. Vatanpour, Preparation of a novel polyvinylidene fluoride (pvdf) ultrafiltration membrane modified with reduced graphene oxide/titanium dioxide (tio2) nanocomposite with enhanced hydrophilicity and antifouling properties, Indust. Eng. Chem. Research 53 (34) (2014) 13370–13382, https://doi.org/10.1021/ie502407g.

[58] Andreas Nahrstedt, Anil Gaba, Barbara Zimmermann, Timo Jentzsch, Kerstin Kroemer, Yannick Tiemann, Lajos Harsanyi, Patrick Buchta, Uli Doelchow, Jens Lipnizki, Katharina Mende, Thomas Koch, Anja Rohn, Reuse of municipal wastewater for different purposes based on a modular treatment concept, J. Water Reuse. Desalinat. 10 (4) (2020) 301–316.

[59] T. Uragami, Science and technology of separation membranes, Wiley Online, Library (2017).

[60] J.C. Birnbaum, T.O. Danby, T.J. Johnson, M.R.K. Kelly-Gorham, R. Lindenmaier, T. L. Myers, PNNL Solid Phase IR Spectra, Pacific Northwest National Laboratory (PNNL) (2017).

[61] A.Z. Hezave, F. Esmaeilzadeh, The effects of RESS parameters on the diclofenac particle size, Adv. Powder Technol. 22 (5) (2011) 587–595, https://doi.org/10.1016/j.apt.2010.08.010.

[62] J.W. Groenendaal, E.J.A.M. Leenderts, T. Van Der Does, Crystalline amoxicillin trihydrate powder, Google Patents (2009).

[63] S.P. Mezyk, E.M. Abud, K.L. Swancutt, G. McKay, D.D. Dionysiou, Removing steroids from contaminated waters using radical reactions, contaminants of emerging concern in the environment ecological and human health considerations, Am. Chem. Soc. (2010) 213–225, https://doi.org/10.1021/bk-2010-1048.ch009.

[64] H. Yu, E. Nie, J. Xu, S. Yan, W.J. Cooper, W. Song, Degradation of diclofenac by advanced oxidation and reduction processes: kinetic studies degradation pathways and toxicity assessments, Water Research 47 (5) (2013) 1909–1918, https://doi.org/10.1016/j.watres.2013.01.016.

[65] R. Andreozzi, M. Canterino, R. Marotta, N. Paxeus, Antibiotic removal from wastewaters: The ozonation of amoxicillin, J. Hazar. Mater. 122 (3) (2005) 243–250, https://doi.org/10.1016/j.jhazmat.2005.03.004.

[66] F Javier Benitez Francisco J Real Juan L Acero Gloria Roldan Removal of selected pharmaceuticals in waters by photochemical processes 84 8 2009 1186 1195 10.1002/jctb.2156.

[67] Munir Cheryan, in: Food Properties and Computer-Aided Engineering of Food Processing Systems, Springer Netherlands, Dordrecht, 1989, pp. 367–391, https://doi.org/10.1007/978-94-009-2370-6_31.

[68] K.H. Chu, M. Fathizadeh, M. Yu, J.R.V. Flora, A. Jang, M. Jang, C.M. Park, S.S. Yoo, N. Her, Y. Yoon, Evaluation of removal mechanisms in a graphene oxide-coated ceramic ultrafiltration membrane for retention of natural organic matter, pharmaceuticals, and inorganic salts, ACS Appl. Mater. Inter. 9 (46) (2017) 40369–40377, https://doi.org/10.1021/acsami.7b14217.

[69] Z. Xu, T. Wu, J. Shi, K. Teng, W. Wang, M. Ma, J. Li, X. Qian, C. Li, J. Fan, Photocatalytic antifouling PVDF ultrafiltration membranes based on synergy of graphene oxide and TiO2 for water treatment, J. Mem. Sci. 520 (2016) 281–293, https://doi.org/10.1016/j.memsci.2016.07.060.

[70] I. Michael-Kordatou, C. Michael, X. Duan, X. He, D.D. Dionysiou, M.A. Mills, D. Fatta-Kassinos, Dissolved effluent organic matter: Characteristics and potential implications in wastewater treatment and reuse applications, Water Research 77 (2015) 213–248, https://doi.org/10.1016/j.watres.2015.03.011.

[71] I. Michael, E. Hapeshi, V. Osorio, S. Perez, M. Petrovic, A. Zapata, S. Malato, D. Barceló, D. Fatta-Kassinos, Solar photocatalytic treatment of trimethoprim in four environmental matrices at a pilot scale: Transformation products and ecotoxicity evaluation, Sci. Total Environ. 430 (2012) 167–173, https://doi.org/10.1016/j.scitotenv.2012.05.003.

[72] A. Azaïs, J. Mendret, E. Petit, S. Brosillon, Evidence of solute-solute interactions and cake enhanced concentration polarization during removal of pharmaceuticals from urban wastewater by nanofiltration, Water Research 104 (2016) 156–167, https://doi.org/10.1016/j.watres.2016.08.014.